# Enhanced tissue regeneration through immunomodulation of angiogenesis and osteogenesis with a multifaceted nanohybrid modified bioactive scaffold

Hang Xue [a,b,1], Zhenhe Zhang [a,b,1], Ze Lin [a,b,1], Jin Su [a,c,1], Adriana C. Panayi [d], Yuan Xiong [a,b], Liangcong Hu [a,b], Yiqiang Hu [a,b], Lang Chen [a,b], Chenchen Yan [a,b], Xudong Xie [a,b], Yusheng Shi [c], Wu Zhou [a,b], Bobin Mi [a,b,**], Guohui Liu [a,b,*]

[a] Department of Orthopaedics, Union Hospital, Tongji Medical College, Huazhong University of Science and Technology, Wuhan, 430022, China
[b] Hubei Province Key Laboratory of Oral and Maxillofacial Development and Regeneration, Wuhan, 430022, China
[c] State Key Laboratory of Materials Processing and Die & Mould Technology, School of Materials Science and Engineering, Huazhong University of Science and Technology, Wuhan, 430074, China
[d] Division of Plastic Surgery, Brigham and Women's Hospital, Harvard Medical School, Boston, MA, 02215, USA

## ARTICLE INFO

## ABSTRACT

Major traumatic tissue defects are common clinical problems often complicated by infection and local vascular dysfunction, processes which hinder the healing process. Although local application of growth factors or stem cells through various tissue engineering techniques are promising methods for the repair of tissue defects, limitations in their clinical application exist. Herein, we synthesized multifaceted nanohybrids composed of Quaternized chitosan (QCS), Graphene oxide (GO), and Polydopamine (PDA; QCS-GO-PDA). Covalent grafting of QCS and GO at a mass ratio of 5:1 (5QCS-1GO) displayed excellent biocompatibility and enhanced osteogenic ability, while addition of PDA (5QCS-1GO-PDA) reduced the level of reactive oxygen species (ROS). 5QCS-1GO-PDA was able to achieve wound tissue regeneration by reducing the inflammatory response and enhancing angiogenesis. Furthermore, Polylactic acid/hydroxyapatite (PLA/HA) composite scaffolds were printed using Selective Laser Sintering (SLS) and the hybrid nanomaterial (5QCS-1GO-PDA) was used to coat the PLA/HA scaffold (5QCS-1GO-PDA@PLA/HA) to be used for rapid bone regeneration. 5QCS-1GO-PDA not only improved angiogenesis and osteogenic differentiation, but also induced M2-type polarization of macrophages and promoted bone regeneration via the BMP2/BMPRs/Smads/Runx2 signaling pathway. The bidirectional enhanced healing ability of the multifaceted nanohybrids 5QCS-1GO-PDA provides a promising method of effectively treating tissue defects.

## 1. Introduction

Effective tissue reconstruction of skin or bone defects following trauma, infection, pathology or excision of lesions is an international clinical challenge [1–3]. Tissue repair and regeneration are complex processes, requiring activation of the immune system and efficient cell proliferation and migration. As a significant component of the peripheral immune response, macrophages play an important regulatory role by responding to different microenvironments. Macrophages can be subdivided into M1 and M2 types according to their activation pathways and secreted products [4]. M1-type macrophages induce excessive fibrosis and healing disorders by secreting pro-inflammatory cytokines, while M2 macrophages promote angiogenesis and osteogenic differentiation through secretion of anti-inflammatory and tissue repair

cytokines such as interleukin-10 (IL-10), transforming growth factor-β (TGF-β), bone morphogenetic protein 2 (BMP2) and vascular endothelial growth factor (VEGF) [5]. Therefore, a shift in the polarization of macrophages from M1 to M2 affects the inflammatory response around biomaterials, creating a microenvironment conducive to tissue regeneration. Endothelium-mediated angiogenesis is considered to be a major pathway for the repair and regeneration of different tissues, as it enables the exchange of oxygen and nutrients and brings growth factors to tissue defects [6]. VEGF is a major participant in angiogenesis, which can stimulate the migration and proliferation of endothelial cells by regulating the released growth factor and paracrine signal, and indirectly stimulate osteogenesis [7]. VEGF and BMP2 have been shown to be the most effective cytokines in promoting angiogenesis and bone formation, respectively, while BMP2 can indirectly promote angiogenesis by stimulating VEGF [7,8]. Studies have shown that vascular development and osteogenesis are coupled in bone formation, suggesting that there is molecular crosstalk between endothelial cells and osteoblasts, and that immune cells regulate this crosstalk effect [9,10]. Recent advances have shown that by tuning the surface properties of materials, such as by incorporating bioactive coatings, it is possible to modulate the functions of a variety of cells. Researchers should optimize tissue-engineered scaffolds with relevant bioactive materials to reproduce the natural repair process and promote tissue regeneration.

Current treatment of tissue defects mainly revolves around autotransplantation, allotransplantation and tissue engineering [11,12]. Although autologous transplantation is the clinical gold standard, it has important disadvantages such as limited donor tissue, size mismatch and injury of the donor site. Allogeneic transplantation on the other hand may carry risks such as disease transmission and immune rejection. Tissue engineering method, such as addition of various growth factors into scaffolds has been tested in the treatment of tissue defects, but growth factors carry disadvantages such as short half-life, high price, and possible toxicity and tumorigenicity. Due to the short half-life and lack of suitable delivery vectors, growth factors are easily degraded and inactivated *in vivo*, which also leads to the frequent use of supraphysiological doses of growth factors as a remedy, resulting in multiple complications in patients [13]. Similarly, application of stem cells can lead to adverse reactions and is limited due to various ethical challenges [14]. Therefore, the design and development of bioactive composite scaffolds which can be custom printed to fully fill a defect cavity and can regulate wound and bone regeneration without the need for cells and growth factors can revolutionize clinical practice.

Studies have shown that quaternized chitosan (QCS), a water-soluble chitosan derivative with enhanced antibacterial effect, has good biocompatibility and can induce tissue repair and regeneration [11,15]. QCS has strong tissue adhesive properties due to positively charged cations in its amino and quaternary amine groups, in addition to antibacterial, hemostatic and enhanced wound healing properties [16]. Graphene Oxide (GO) is a two-dimensional material with a wide range of properties, including high surface area, and inherent antibacterial, angiogenic and osteogenic abilities [17]. Polydopamine (PDA) is polymerized by dopamine, and forms a functional polymer layer on various materials, including polymers, ceramics, and metals. Some studies have shown that PDA can significantly promote osteoblast proliferation and adhesion, and promote angiogenesis [18]. Selective Laser Sintering (SLS) is one of the most important technologies in the field of 3D printing (additive manufacturing). Compared with traditional methods, SLS can provide personalized printing for different patients and has broad application prospects [19]. As a biodegradable material, Polylactic acid (PLA) can be 3D printed into tissue scaffolds, which can be combined with Hydroxyapatite (HA), the main component of bone matrix, to effectively improve the biological activity of scaffolds [20]. However, combination of PLA/HA and SLS forming technology has not been well studied. Therefore, we speculated that a complex composed of GO, QCS and PDA can promote rapid tissue regeneration, and in combination with PLA/HA scaffold and SLS technology allow personalized custom printing for diverse bone defects. In addition, through the simple combination of nanocomposites and tissue-engineered scaffolds, this multifunctional platform can be widely used for tissue regeneration and repair.

In this study, we synthesized and characterized a nanohybrid composed of QCS, GO, and PDA (QCS-GO-PDA), and investigated its repair abilities on tissue defects. In a full-thickness skin defect, QCS-GO-PDA was able to accelerate wound healing and induce skin regeneration. In a bone defect model, PLA/HA composite scaffolds were printed using SLS, QCS-GO-PDA was applied as a coating material and the composite was used to effectively repair critical size calvarial defects. The free catechin groups on the PDA chain and the positively charged amino groups on the QCS offered the nanohybrids adhesive abilities. *In vivo* repair of bone defects highlighted that the synergistic effect of the QCS-GO-PDA@PLA/HA biomimetic scaffold could accelerate the regeneration of bone tissue. The QCS-GO-PDA nanomaterial is shown to exert multiple functions including promoting cell migration and adhesion, inducing vascular formation and osteogenic differentiation, and is expected to be an effective technique for promoting tissue regeneration in clinical practice (Scheme 1).

## 2. Results

### 2.1. Characterization of the nanohybrids and screening of high cell viability and strong antibacterial effects

Firstly, QCS and GO were synthesized in a mass ratio of 1:1, 3:1, 5:1 and 10:1, and then the corresponding QCS-GO-PDA was synthesized. Four kinds of QCS-GO-PDA nanohybrids were named as 1QCS-1GO-PDA, 3QCS-1GO-PDA, 5QCS-1GO-PDA, 10QCS-1GO-PDA. As shown in Fig. 1A, the synthesized QCS-GO-PDA displayed a typical layered structure with some wrinkled areas and a rough surface under transmission electron microscope (TEM). As shown in Fig. S1, the nanohybrids had an average diameter of $274.42 \pm 133.03$ nm.

The chemical structure and functional groups of QCS and the synthesized QCS-GO and QCS-GO-PDA were detected under Fourier-transform infrared (FTIR) spectroscopy. As shown in Fig. 1B, the characteristic peak of QCS at 1480 cm$^{-1}$ is the stretching vibration of C–H bond, indicating that glyceryl trimethyl ammonium chloride (GTMAC) was successfully grafted onto chitosan. The peak at 1550 cm$^{-1}$ which corresponds to the newly formed –NHCO - bond between QCS and GO, appears in the QCS-GO and QCS-GO-PDA spectra, but is not seen in the GO spectra, confirming that the QCS molecule has been grafted to GO via an amide bond. Thermogravimetric analysis (Fig. S2) of GO showed that 6% of its weight was lost below 100 °C due to evaporation of adsorbed water. The main weight loss of GO was between 185 and 255 °C, probably due to thermal degradation of oxygen-containing groups. The weight loss rate of QCS was less than 5% below 100 °C and 40% between 245 and 285 °C. The weight loss curve of QCS-GO mainly consisted of two stages, the main loss of GO (185–235 °C) and QCS (260–290 °C). The weight loss curve of QCS-GO-PDA showed changes in three stages, respectively in (115–195 °C), (215–265 °C) and (285–415 °C), which correspond to the composition of the nanohybrids. Scanning electron microscopy (SEM) showed that QCS-GO and QCS-GO-PDA had a microporous structure after freeze-drying (Fig. 1C), while QCS had a dendritic rough surface structure with uneven pore distribution. EDS mapping showed the distribution of three main elements C, O and Cl.

The concentration gradient of 25–125 μg/mL was selected to detect cell viability of four kinds of nanohybrids. After co-culture with human umbilical vein endothelial cells (HUVECs), the cell survival rate of QCS and GO at different mass ratios was determined by CCK-8 kit. As shown in Fig. 1D, all four proportions of QCS-GO-PDA showed good cell viability in the selected concentration range, among which 5QCS-1GO-PDA and 10QCS-1GO-PDA showed the highest cell survival. The cell viability of the 5QCS-1GO-PDA and 10QCS-1GO-PDA gradually
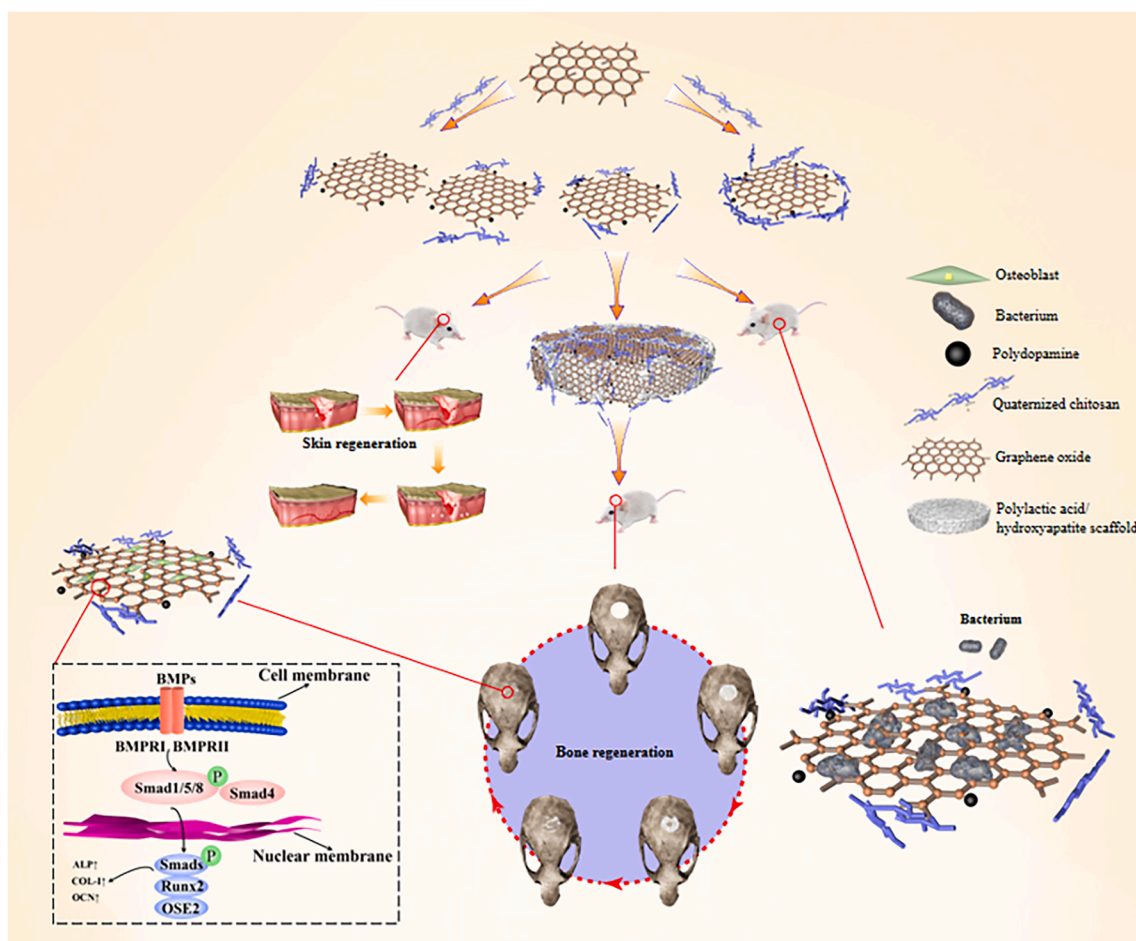
**Scheme 1.** Schematic diagram of the proposed mechanism of tissue repair and regeneration induced by 5QCS-1GO-PDA and 5QCS-1GO-PDA@PLA/10%HA scaffold.

increased from 25 µg/mL, reaching the highest value of 75 µg/mL, and gradually decreased after 100 µg/mL. At the same time, we found that other groups also showed a similar trend, suggesting that the concentration of about 75 µg/mL QCS-GO-PDA could be the least toxic to cells, a phenomenon more obvious with 5QCS-1GO-PDA.

Three common microorganisms *Staphylococcus aureus (S. aureus), Staphylococcus epidermidis (S. epidermidis), Escherichia coli (E. coli)* were selected to test the antibacterial activity of QCS-GO-PDA. In order to obtain the nanohybrids with optimal cell viability and antibacterial ability, we selected the concentration at a relatively higher cell viability (75 µg/mL) to continue the antibacterial experiment. As shown in Fig. 1E, with the increase in QCS to GO ratio, the antibacterial ability of the QCS-GO-PDA gradually increased, and the increase was more obvious when QCS-GO increased from 1:1 to 3:1, and the bactericidal rate gradually stabilized at 5:1. 5QCS-1GO-PDA and 10QCS-1GO-PDA showed relatively similar antibacterial activity ($p > 0.05$, no significant difference , Fig. 1F–H). As shown in Fig. 1I, the morphological changes of *S. aureus* without any treatment in the control group was smooth and almost circular, while the cell surface of *S. aureus* treated with QCS was wrinkled. The morphological changes of *S. aureus* treated by QCS-GO were more drastic, and the wrinkling phenomenon was more obvious, with collapse and shape changes appearing, indicating the existence of physical damage. *S. aureus* treated with QCS-GO-PDA showed similar changes to QCS-GO, that was, the morphology of the bacteria showed wrinkling and irregular changes. The quaternary ammonium group and the positively charged amino group in QCS were effective in killing bacteria. As previously mentioned, it can be concluded that 5QCS-1GO-PDA has both good cell viability and stronger bactericidal performance compared with the other three groups, among

which the cell viability is optimal when the concentration is around 75 µg/mL. Therefore, subsequent studies focused on 5QCS-1GO-PDA and the effect of the sequential addition of GO and PDA on the biological function of nanohybrids will be further investigated. Cell viability analyses of vascular endothelial cells, MC3T3-E1 and RAW 264.7 cells treated with different concentrations of QCS, 5QCS-1GO, 5QCS-1GO-PDA were shown in Fig. S3. This showed that the optimal concentrations of the three cells mentioned above were mainly distributed between 50 and 100 µg/mL.

### 2.2. HUVECs proliferation, migration and angiogenesis induced by nanohybrids

Angiogenesis plays an important role in the repair of traumatic tissue defects. The establishment of vascular network delivers nutrients and growth factors to the defect area, which is permissive to rapid repair. As shown in Fig. 2A, 5QCS-1GO-PDA, 5QCS-1GO and QCS were co-cultured with HUVECs at 75 µg/mL for 1, 3 and 5 days. The morphology of cells was analyzed with calcein-AM staining. The results showed that all three groups (QCS, 5QCS-1GO, and 5QCS-1GO-PDA) had promoting effects on cell proliferation, with 5QCS-1GO-PDA inducing the highest cell proliferation rate. EdU staining showed that 5QCS-1GO-PDA was the most effective at promoting cell proliferation in all groups (Fig. 2B).

As shown in Fig. 2C–F, compared with the control group, there was no significant difference in the cytoskeleton staining of HUVECs in the three groups, the cell morphology was relatively regular and the cytoskeleton was intact, suggesting that addition of different components had no obvious effect on the state of endothelial cells. *In vitro* scratch assay indicated that compared with the other three groups, 5QCS-1GO-
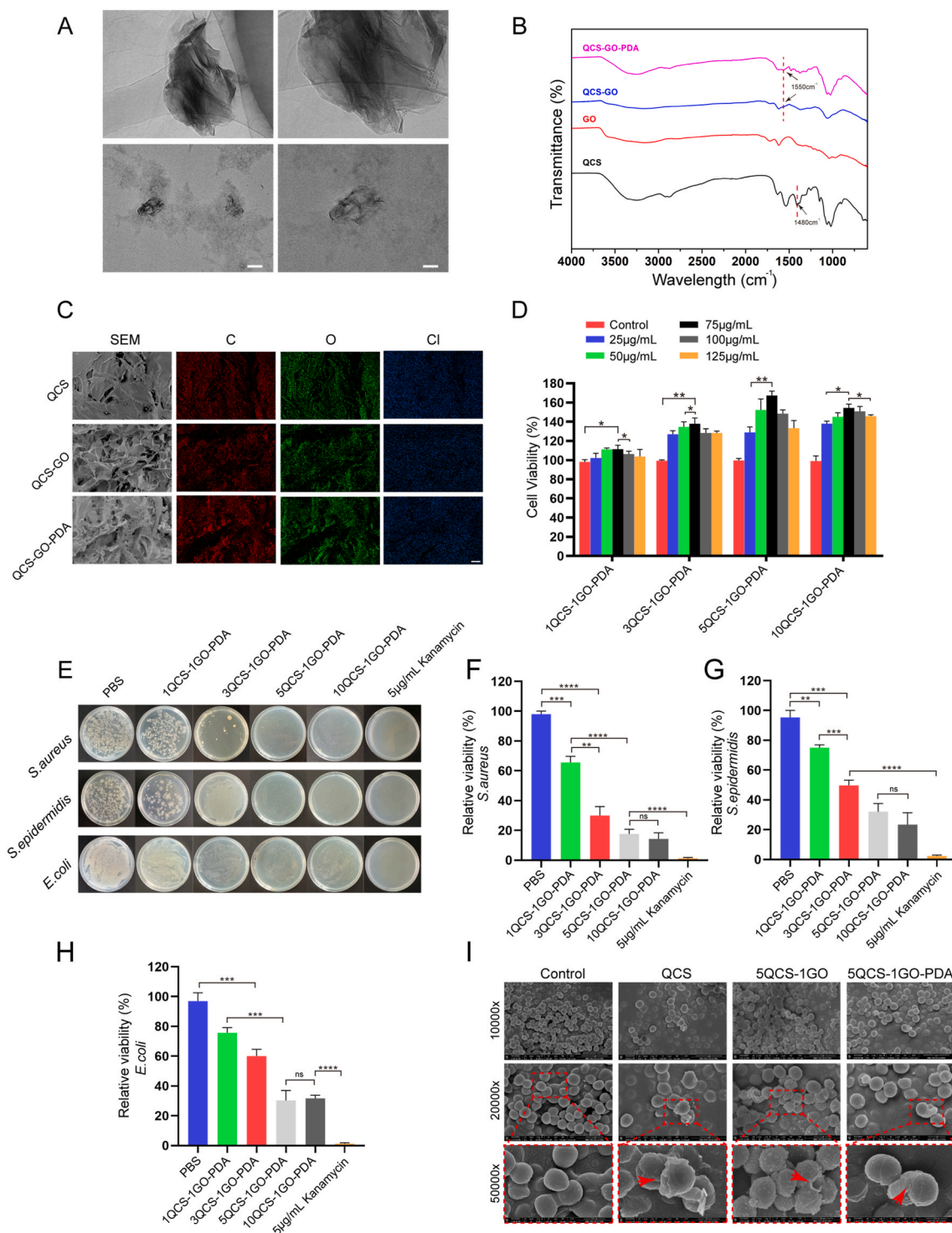
**Fig. 1.** Characterization of the nanohybrids and screening of high cell viability and strong antibacterial effects. (A) Representative TEM images of the QCS-GO-PDA. Scale bar: 200 nm (left) and 100 nm (right). (B) FTIR of QCS/GO/QCS-GO/QCS-GO-PDA. (C) SEM and EDS mapping after freeze drying of QCS, QCS-GO and QCS-GO-PDA. Scale bar: 50 μm. (D) Cell viability analysis of QCS-GO-PDA containing different proportions of QCS/GO. (E–H) Representative images and quantitative analysis of antibacterial ability of the different proportions of QCS-GO-PDA (*S. aureus*, *S. epidermidis* and *E. coli*). (I) After being treated with QCS, 5QCS-1GO and 5QCS-1GO-PDA for 2 h, the morphological changes of *S. aureus* were observed. Scale bar: 3 μm (top), 1 μm (middle) and 500 nm (bottom). Data are represented as mean ± SD ($n = 3$, *$p < 0.05$, **$p < 0.01$, ***$p < 0.001$, ****$p < 0.0001$).

PDA significantly improved the migration ability of endothelial cells, which is very important for enhancing wound healing. A transwell assay showed that the migration ability of endothelial cells in the 5QCS-1GO-PDA group was superior to the other groups and was beneficial to the formation of blood vessels during repair, a phenomenon which may be

related to the fact that PDA promoted cell adhesion and improved angiogenesis, and the migration ability of QCS and 5QCS-1GO was weaker than that of 5QCS-1GO-PDA. In addition, we conducted a further tube formation experiment with the three groups and observed blood vessel formation, identifying that 5QCS-1GO-PDA had the strongest
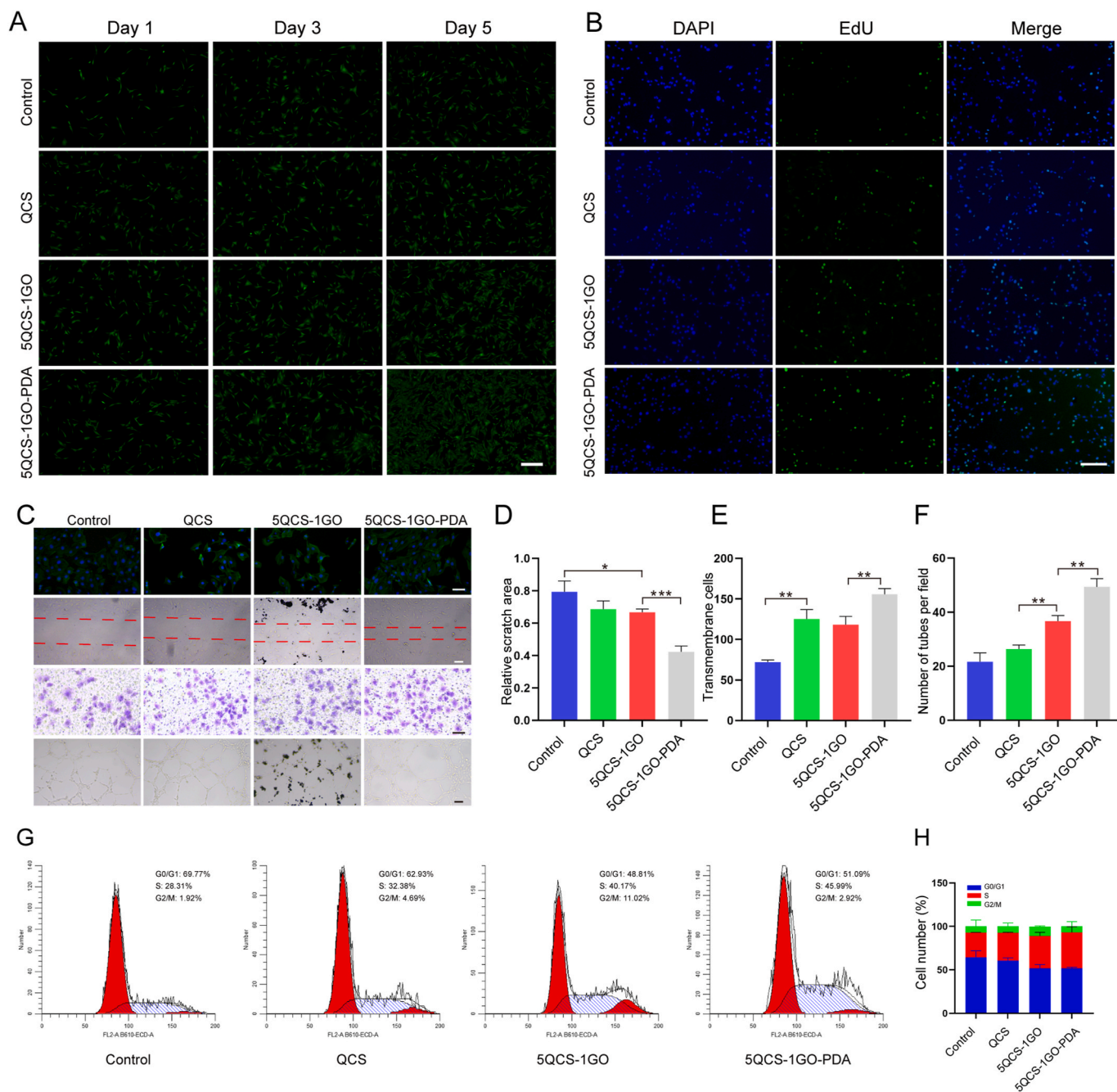
**Fig. 2.** Proliferation, migration and angiogenesis of endothelial cells induced by nanohybrids and their different components. (A) The effects of QCS, 5QCS-1GO and 5QCS-1GO-PDA on endothelial cells proliferation and calcein-AM staining analysis. Scale bar: 200 μm. (B) The effects of 5QCS-1GO-PDA and QCS, 5QCS-1GO on the proliferation of endothelial cells were evaluated by EdU incorporation. Scale bar: 100 μm. (C–F) Cytoskeleton staining, scratch assay, transwell assay and tube formation were used to detect the effects of nano-hybrid compounds on migration and angiogenic ability of endothelial cells. Scale bar: 50 μm. (G–H) Cell cycle determination of the effect of nanohybrids on the cycle distribution of endothelial cells by flow cytometry. Data are represented as mean ± SD ($n = 3$, $*p < 0.05$, $**p < 0.01$, $***p < 0.001$).

angiogenic ability. The tube formation of endothelial cells in the 5QCS-1GO group was stronger than that in the QCS group. As shown in Fig. 2G–H, the results of cell cycle distribution quantified by flow cytometry showed that the proportion of cells entering S phase increased significantly after 5QCS-1GO-PDA treatment compared with the control group.

### 2.3. Effect of 5QCS-1GO-PDA on ROS scavenging capacity and macrophage polarization

As shown in Fig. 3A, there were very few fluorescent dyes in the

control group, indicating that RAW 264.7 cells produced low intracellular ROS levels without any stimulation. As described in previous literature, $H_2O_2$ can induce high intracellular ROS expression in RAW 264.7 cells because $H_2O_2$ can cross the cell membrane and activate macrophages to produce ROS [21]. It was observed that ROS levels in the 5QCS-1GO-PDA group decreased significantly after $H_2O_2$ stimulation, while ROS levels in the other two groups were higher. This is probably mainly due to the antioxidant properties of PDA, and the ROS produced by macrophages can be cleared by PDA, thus reducing the ROS level of macrophages. The results of the co-culture experiment of macrophages showed that 5QCS-1GO-PDA had great antioxidant activity.
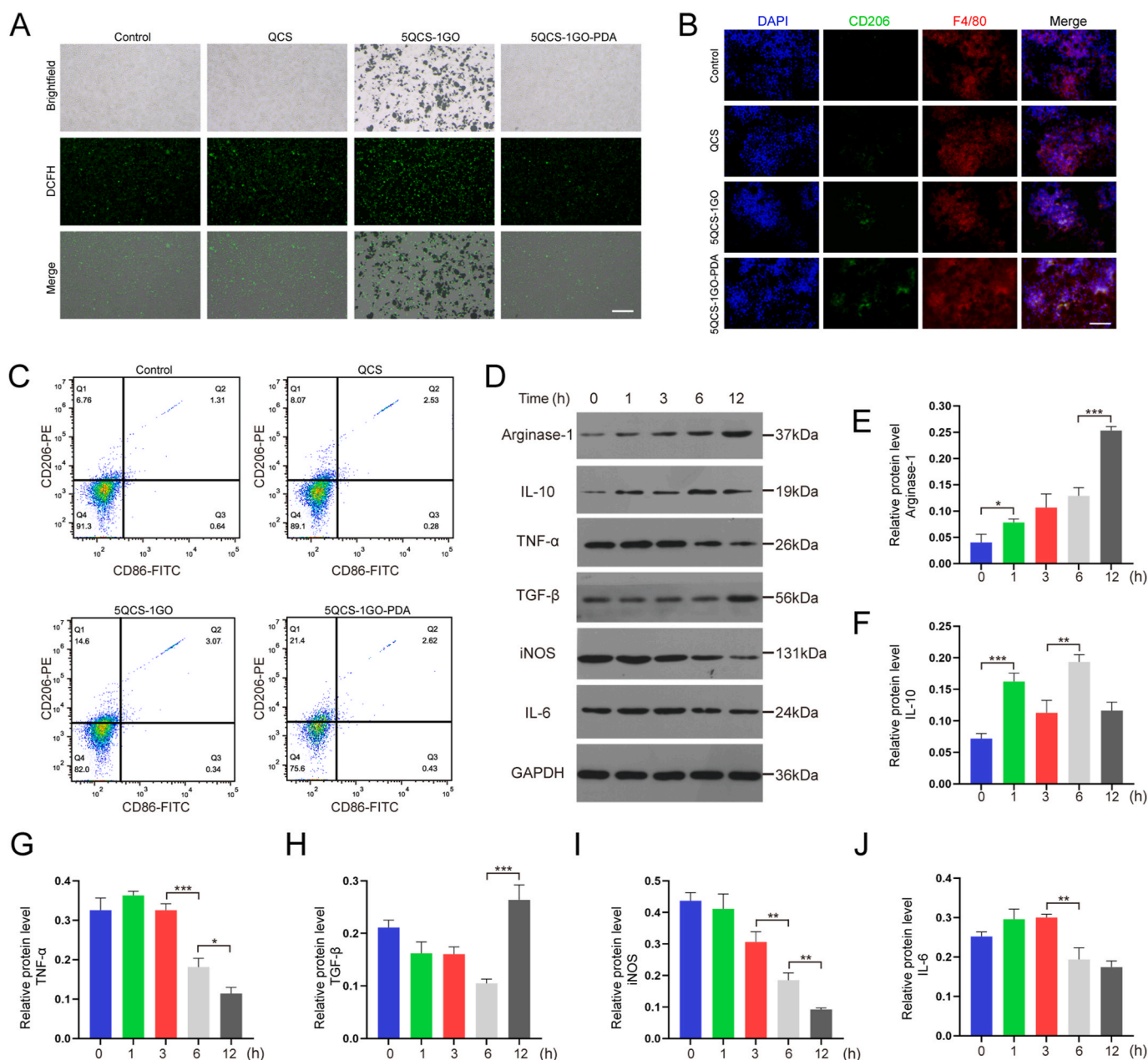
**Fig. 3.** Effect of 5QCS-1GO-PDA on ROS scavenging capacity and macrophage polarization. (A) Changes in intracellular ROS levels of macrophages after oxidative stimulation. Scale bar: 100 μm. (B) CD206 and F4/80 immunofluorescence staining of macrophages treated with QCS, 5QCS-1GO, 5QCS-1GO-PDA for 3 days. Scale bar: 100 μm. (C) Flow cytometry was used to detect the expression of macrophage membrane surface proteins. (D–J) Western blot analysis of the effect of 5QCS-1GO-PDA treatment on secreted products of macrophages. Data are represented as mean ± SD ($n = 3$, $*p < 0.05$, $**p < 0.01$, $***p < 0.001$).

Lower ROS levels provided by 5QCS-1GO-PDA in macrophages will help reduce the intensity of the inflammatory response during repair and promote tissue regeneration.

To determine the effect of 5QCS-1GO-PDA on the polarization of macrophages, 75 μg/mL of QCS, 5QCS-1GO, or 5QCS-1GO-PDA were co-cultured with RAW 264.7 macrophages for three days, and CD206 immunofluorescence staining was performed. As shown in Fig. 3B, the QCS and 5QCS-1GO groups showed the lower fluorescence intensity, while CD206 in the 5QCS-1GO-PDA group had the highest fluorescence intensity, suggesting that the polarization of macrophages to M2 type was most promoted with co-culture with 5QCS-1GO-PDA. Similarly, we detected the expression of the macrophage surface markers CD206 and CD86 using flow cytometry, and the results showed that the expression of CD206 was highest in the 5QCS-1GO-PDA group, consistent with the results of the immunofluorescence staining (Fig. 3C).

In order to further understand the effect of 5QCS-1GO-PDA on macrophages, the proteins of 5QCS-1GO-PDA treated macrophages were quantified at different time points (0, 1, 3, 6 and 12 h), and the expression of related secretions of the macrophages with different polarization types was analyzed (Fig. 3D). The results showed that the expression of Arginase-1 gradually increased with time, especially at 12 h (Fig. 3E). The level of IL-10 showed unstable changes, increasing at 1 and 6 h, then decreasing again at 3 and 12 h, respectively (Fig. 3F). The level of iNOS showed a trend of gradual decline, while the level of IL-6 was relatively stable and declined from 6 h onwards (Fig. 3I–J).

### 2.4. Determination of the osteogenic ability of the nanohybrids and the immune crosstalk between osteogenesis and angiogenesis

The osteogenic ability of tissue engineered materials is very

important for the repair and regeneration of bone defects. As shown in Fig. 4A, the formation of calcium nodules in the QCS, 5QCS-1GO and 5QCS-1GO-PDA groups after alkaline phosphatase staining gradually increased, and the calcium nodules in the 5QCS-1GO-PDA group were significantly stronger than the other two groups. Alizarin red staining of MC3T3-E1 cells after 14 days of osteogenic induction showed that 5QCS-1GO-PDA had the most extracellular calcium deposition, similar to the result of alkaline phosphatase staining (Fig. 4A). As shown in Fig. 4B, Western blot results showed that the osteogenic related proteins runt-related transcription factor 2 (Runx2), alkaline phosphatase (ALP),

osteocalcin (OCN) and collagen-1 (Col-1) were significantly up-regulated in the 5QCS-1GO and 5QCS-1GO-PDA groups compared to the control group. The expression of ALP protein was nearly 1.5 times higher in the 5QCS-1GO-PDA than that of QCS. The expression of OCN in the 5QCS-1GO-PDA and 5QCS-1GO groups was three times higher than that in the control group. Western blot results showed that treatment of MC3T3-E1 cells with 5QCS-1GO and 5QCS-1GO-PDA significantly enhanced the expression of BMP2, BMPR1B and BMPR2, and increased phosphorylation level of Smad1/5/8 (Fig. S4).

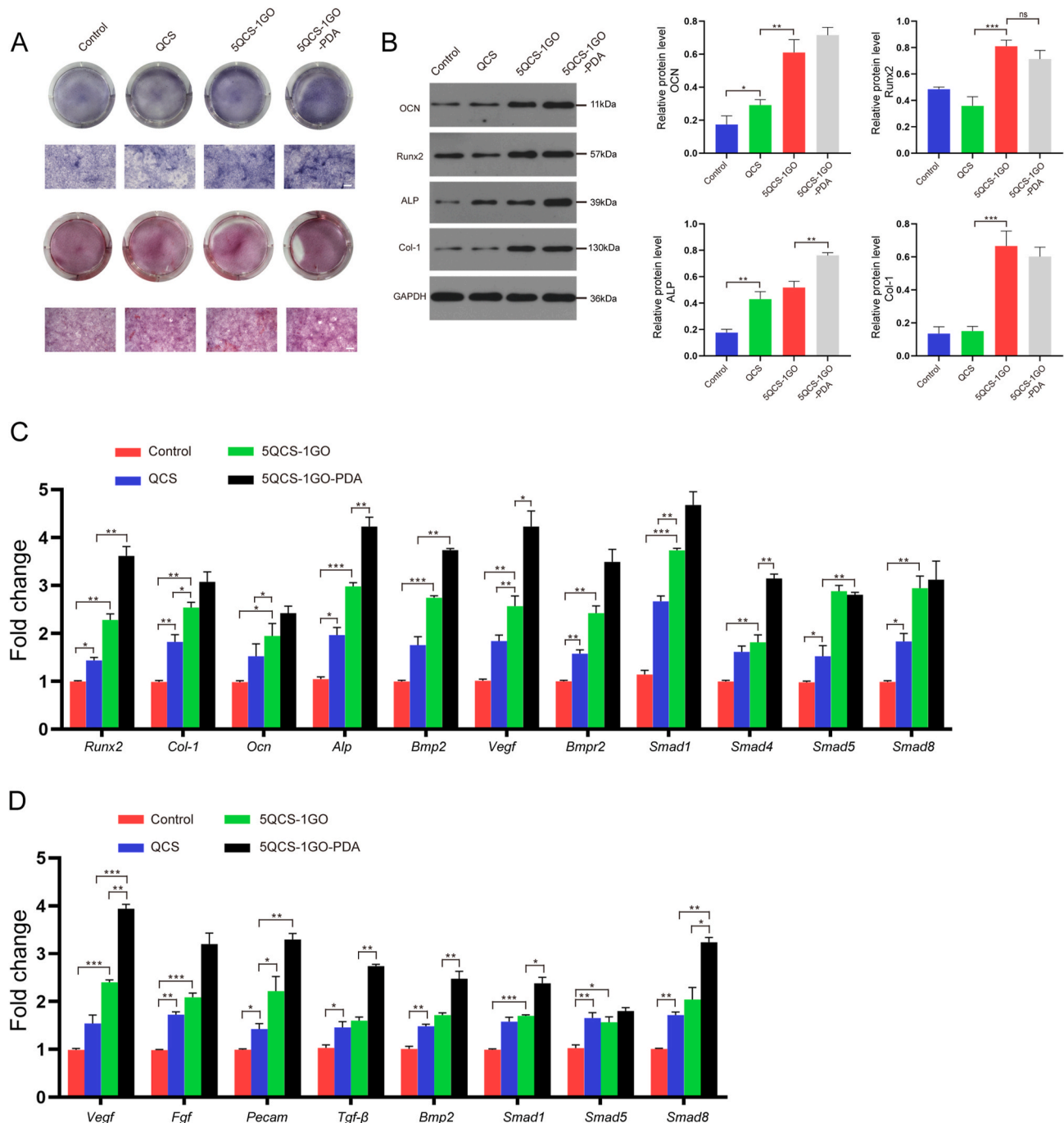To study the immunomodulatory regulation on bone formation and



**Fig. 4.** Determination of the osteogenic ability of the nanohybrids and the immune crosstalk between osteogenesis and angiogenesis. (A) Alkaline phosphatase and alizarin red staining following 14 days of co-culture with MC3T3-E1. Scale bar: 50 μm. (B) Western blot analysis of osteogenic related protein expression. (C) The influence of osteogenesis related gene expression in MC3T3-E1 cells cultured for 3 days detected by qRT-PCR. (D) qRT-PCR was used to detect the effects of a macrophage conditioned medium on the expression of angiogenesis-related genes in HUVECs cultured in QCS/5QCS-1GO/5QCS-1GO-PDA conditioned medium for 3 days. Data are represented as mean ± SD ($n = 3$, *$p < 0.05$, **$p < 0.01$, ***$p < 0.001$).

angiogenesis, conditioned culture medium of macrophages treated with QCS, 5QCS-1GO or 5QCS-1GO-PDA was collected and applied to the culture of osteoblasts and vascular endothelial cells. The results showed that *Runx2, Bmp2, Alp* and *Smads* gene expression were up-regulated in MC3T3-E1 cells cultured in the 5QCS-1GO-PDA-conditioned macrophage medium (Fig. 4C). In this study, we also found that macrophage conditioned medium co-cultured with 5QCS-1GO and 5QCS-1GO-PDA had significantly higher expression of angiogenesis related genes, which was particularly evident with 5QCS-1GO-PDA. The gene expression of *Vegf*, fibroblast growth factor (*Fgf*), *Tgf-β* and *Bmp2* was significantly up-regulated (Fig. 4D). These results suggest that there is an interaction between osteoblasts and vascular endothelial cells, and that 5QCS-1GO-PDA can modulate osteogenesis and angiogenesis by influencing the immune microenvironment. In endothelial cells, *Tgf-β, Vegf, Bmp2* gene expression was significantly up-regulated in the 5QCS-1GO-PDA group. In addition, the expression of the *Fgf* and platelet endothelial cell adhesion molecule (*Pecam*) genes, associated with endothelial cell migration and formation, was also up-regulated in the 5QCS-1GO-PDA group, which was consistent with the results of the transwell assay and tube formation above-mentioned. Based on the above research, there is convincing evidence that 5QCS-1GO-PDA not only directly affects the functions of macrophages, osteoblasts and endothelial cells, but also synergistically regulates their interactions while promoting osteogenesis and angiogenesis, which has important implications for osseointegration *in vivo*.

### 2.5. Evaluation and histological analysis of full-thickness skin regeneration

In order to analyze the wound healing effect of the different components of the nanohybrids on skin wounds, full-thickness skin defects of Sprague–Dawley rats were treated with QCS, 5QCS-1GO and 5QCS-1GO-PDA. Wound healing at 0, 5, 9 and 14 days after surgery is shown in Fig. 5A. The wound area of different groups showed a trend of gradually decreasing with time. Among all groups, the wound closure speed of the 5QCS-1GO-PDA group was the highest. As shown in Fig. 5B, the wound healing rate of the 5QCS-1GO-PDA group reached 80% at nine days after surgery, and the wound almost completely healed at 14 days after surgery. From Fig. 5C it is evident that the untreated control group healed the slowest.

Subsequently, we further analyzed the wound repair effect of QCS, 5QCS-1GO and 5QCS-1GO-PDA at the histological level. We performed hematoxylin and eosin (H&E) staining and Masson's trichrome staining on skin tissue samples post healing to further understand the effects of the different treatment groups on wound healing. Histological staining showed that the 5QCS-1GO-PDA promoted the formation of skin tissue and its appendages. As shown in Fig. 5D, the maximum granulation tissue spacing of the wound in the control group was 3260 μm, while granulation tissue spacing was reduced to 1930 μm in the QCS-treated wounds, and further reduced to 1300 μm in the 5QCS-1GO group. The granulation tissue of the 5QCS-1GO-PDA group was 833 μm, which was the smallest. In addition, Masson's trichrome staining showed regular collagen arrangement in the 5QCS-1GO-PDA treatment group, which
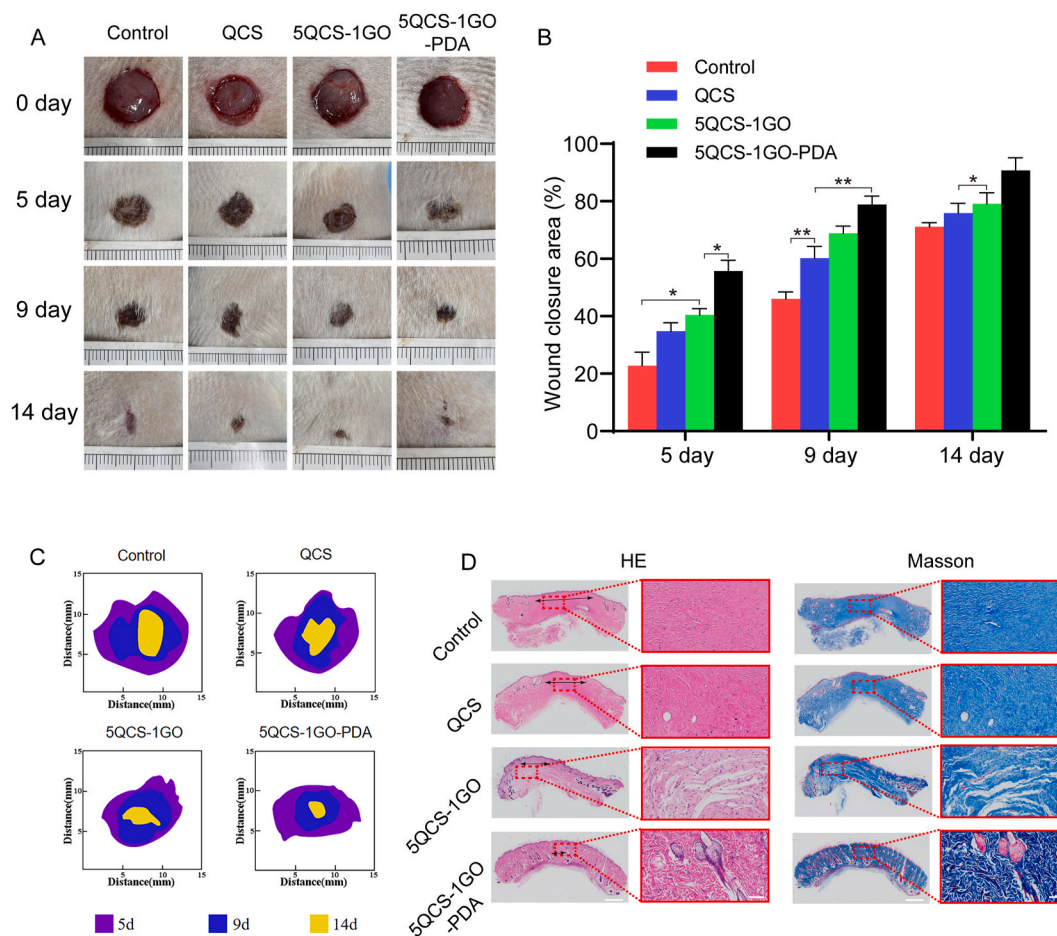


**Fig. 5.** Evaluation and histological analysis of full-thickness skin regeneration. (A) Representative photographs of wound healing. (B) Quantitative statistical analysis of the rate of wound healing in the treatment group. (C) Schematic diagram of the wound closure at different time points. (D) H&E staining & Masson's trichrome staining of new skin tissue at day 21 postoperatively. Scale bar: 1 mm or 100 μm. Data are represented as mean ± SD ($n = 5$, $*p < 0.05$, $**p < 0.01$).

further demonstrated the maturity of the regenerated tissue.

Angiogenesis was assessed with immunohistochemistry for CD31 and immunofluorescence staining for CD31 and alpha-smooth muscle actin (α-SMA) in wound tissue at different time points. Quantitative analysis of neovascularization density was determined by the number of CD31-positive cells per square millimeter. As shown in Fig. 6A, on day 9, vascular density was significantly higher in the 5QCS-1GO-PDA group than in the other groups. From day 5 to day 9, all four treatment groups showed increased mature vessel density, but the number of mature vessels was lower than that of neovascularization (Fig. 6B). 9 days after surgery, the number of mature blood vessels in the skin defect area treated with 5QCS-1GO-PDA was significantly higher than that in the control group, QCS group and 5QCS-1GO group. As shown in Fig. 6C, 5 days after surgery, CD68 immunofluorescence staining was performed on the wound tissue, and the fluorescence level of 5QCS-1GO-PDA was the lowest in all groups, indicating a mild inflammatory response, which may be due to the ROS clearance ability of 5QCS-1GO-PDA *in vivo*, that is, the inflammatory response of wound is regulated by inhibiting the ROS level, which is consistent with the aforementioned research results. Immunofluorescence staining for CCR7 (M1 macrophage marker) and CD206 (M2 macrophage marker) was performed to evaluate the expression level in wound tissue 5 and 9 days after treatment. As shown in Fig. S5A, the fluorescence intensity of CD206 was highest in 5QCS-1GO-PDA group, while the fluorescence intensity of CCR7 in 5QCS-1GO-PDA group was lowest. Statistical analysis showed that the M2/M1 ratio in 5QCS-1GO-PDA group was 6 times higher than that in control group on both 5 and 9 days after treatment, indicating that 5QCS-1GO-PDA could promote the polarization of macrophages to M2 type and play an anti-inflammatory role in the wound (Fig. S5B-C).

## 2.6. Surface morphology and biological characteristics of PLA/HA scaffolded by SLS

In this study, PLA and HA with mass fraction of 0%, 10%, 15% and 20% were printed into the tissue engineered scaffold PLA/HA using SLS (Fig. 7A). The four scaffolds with different HA mass ratios were named PLA/0%HA, PLA/10%HA, PLA/15%HA and PLA/20%HA, respectively. Fig. 7B shows the surface microscopic morphology of the PLA/HA composite scaffolds with different HA mass fractions. It can be observed that the surface of the PLA/HA composite melts relatively well after addition of HA. The surface microstructure of the scaffold printed with a 10% mass fraction HA was flat and smooth, and the particle size distribution was uniform. The surface morphology of the composite scaffold was optimal when 10% and 15% HA was added. When the HA mass fraction reaches 20%, the surface of PLA/HA composite becomes uneven possibly because the gradual increase of the HA mass fraction may lead to thermal decomposition of the PLA/HA composites.

The above four scaffolds were treated with MC3T3-E1 cells for 1 day and 3 days, respectively. The results indicated that all four scaffolds showed good cytocompatibility, and the cell viability in the PLA/10% HA group increased more significantly on day 3 (Fig. S6). As shown in Fig. 7C, alkaline phosphatase and alizarine red staining were used to evaluate the calcium nodule formation and extracellular calcium deposition, respectively. PLA/HA (HA = 0%, 10%, 15%, 20%) and MC3T3-E1 cells were co-cultured for 14 days. The results showed that the PLA/HA scaffold with HA = 10% showed the strongest osteogenic ability, followed by PLA/HA scaffolds with HA = 15% and HA = 20%. In addition, we co-cultured four PLA/HA scaffolds with MC3T3-E1 cells for 14 days and detected the expression of osteogenic genes and osteogenic proteins (Fig. 7D–I). qRT-PCR and western blotting indicated that PLA/ HA with HA = 10% showed the higher osteogenic ability, consistent with the results of prior staining. This indicates that PLA/HA is most suitable for SLS printing when the HA equals 10%, resulting in a PLA/ HA scaffold with better morphology and hydrophilicity. In conclusion, PLA/10%HA was identified as the optimal choice for use as a bone repair scaffold from the four PLA/HA mass ratios.

PLA/10%HA was co-cultured with MC3T3-E1 cells, and the cell morphology distributed on the surface was observed with SEM. It can be seen from Fig. 7J that MC3T3-E1 cells have good spreading and adhesion, and are distributed in different positions of the scaffold with good morphology, some of which cling to the particles on the surface of the scaffold, while others are inserted into the pores of the scaffold. The viability of MC3T3-E1 cells cultured on the scaffolds were evaluated by confocal laser microscopy at 3 days after cell seeding (Fig. 7K-L). The cell survival rate of PLA/10%HA scaffold was higher than that of the other groups. These results showed that the cells on PLA/10%HA were in a good state which was conducive to the proliferation and differentiation of osteoblasts, indicating PLA/10%HA was a promising choice as a scaffold for bone defect repair. *In vitro* degradation experiments, the PLA/0%HA scaffolds remained stable during the first month and showed no obvious degradation. The degradation rates of the other three groups also showed low during the first month. From month 2 onwards, weight loss was more rapid in the PLA/10%HA and PLA/20%HA groups, approximately equal to 15–20% of the initial weight. The residual weight of the PLA/15%HA at day 60 was similar to that of the PLA/10% HA scaffold, but the degradation trend began to slow down (Fig. S7).

## 2.7. Histological analysis of the repair of critical size bone defects in rats

To investigate whether nanohybrids and composite scaffolds printed by SLS could synergistically enhance bone regeneration, QCS, 5QCS-1GO and 5QCS-1GO-PDA were used as coating materials for PLA/10% HA scaffolds (QCS@PLA/10%HA, 5QCS-1GO@PLA/10%HA, 5QCS-1GO-PDA@PLA/10%HA) to study the reparative effects on critical bone defects in rats. Micro-CT was used to evaluate the repair efficacy of the scaffolds in critical-sized rat cranial defects at 4 and 12 weeks after composite scaffold implantation. As shown in Fig. 8A, more new bone formation was observed in the 3D reconstruction and coronal images in the 5QCS-1GO-PDA@PLA/10%HA 4 weeks after implantation. Meanwhile, no significant differences were observed between PLA/10%HA and QCS@PLA/10%HA. However, when the treatment period was extended to 12 weeks, the 5QCS-1GO@PLA/10%HA and 5QCS-1GO-PDA@PLA/10%HA groups showed more new bone tissue than the other groups in the CT reconstruction and coronal images (Fig. 8B). Quantitative analysis showed that the bone volume (BV) (Fig. 8C), bone volume/total volume (BV/TV) ratio (Fig. 8D) of the 5QCS-1GO@PLA/10% HA and 5QCS-1GO-PDA@PLA/10%HA groups were more than 1.5 times higher than those of the other two groups, especially in 5QCS-1GO-PDA@PLA/10%HA. Four weeks after implantation, H&E staining and Masson's trichrome staining of the scaffold in the four groups (Fig. 9A), showed that the new bone tissue had bony spaces and central canals, with significantly more bone tissue observed in the 5QCS-1GO-PDA@-PLA/10%HA group. 12 weeks after implantation, mature and dense bone tissue was observed at the edges of the four groups using H&E staining and Masson's trichrome staining (Fig. 9B). The 5QCS-1GO@PLA/10%HA and 5QCS-1GO-PDA@PLA/10%HA groups had the greatest level of filling of the bone defects with newly formed bone tissue, while the other two groups had only partial bone formation. Collagen deposition was increased in the defect sites filled with 5QCS-1GO-PDA@PLA/10%HA compared to the other groups. In the methylene acid fuchsin staining, different degrees of new bone formation were observed around the scaffolds in all four groups, and the increase of new bone tissue in the 5QCS-1GO-PDA group was significantly higher at the scaffold-bone interface than that in the other three groups, which was in accordance with the H&E and Masson's trichrome staining results (Fig. S8). To evaluate how scaffolds affect macrophage polarization, immunofluorescence staining for CCR7 and CD206 in bone defect regions was performed. As shown in Fig. S9A, the fluorescence intensity of CD206 was highest in 5QCS-1GO-PDA@PLA/10%HA scaffold group at 4 and 12 weeks after surgery. However, the number of macrophages expressing CCR7 was least compared to that of other three groups. Statistical analysis showed that the M2/M1 ratio in 5QCS-1GO-
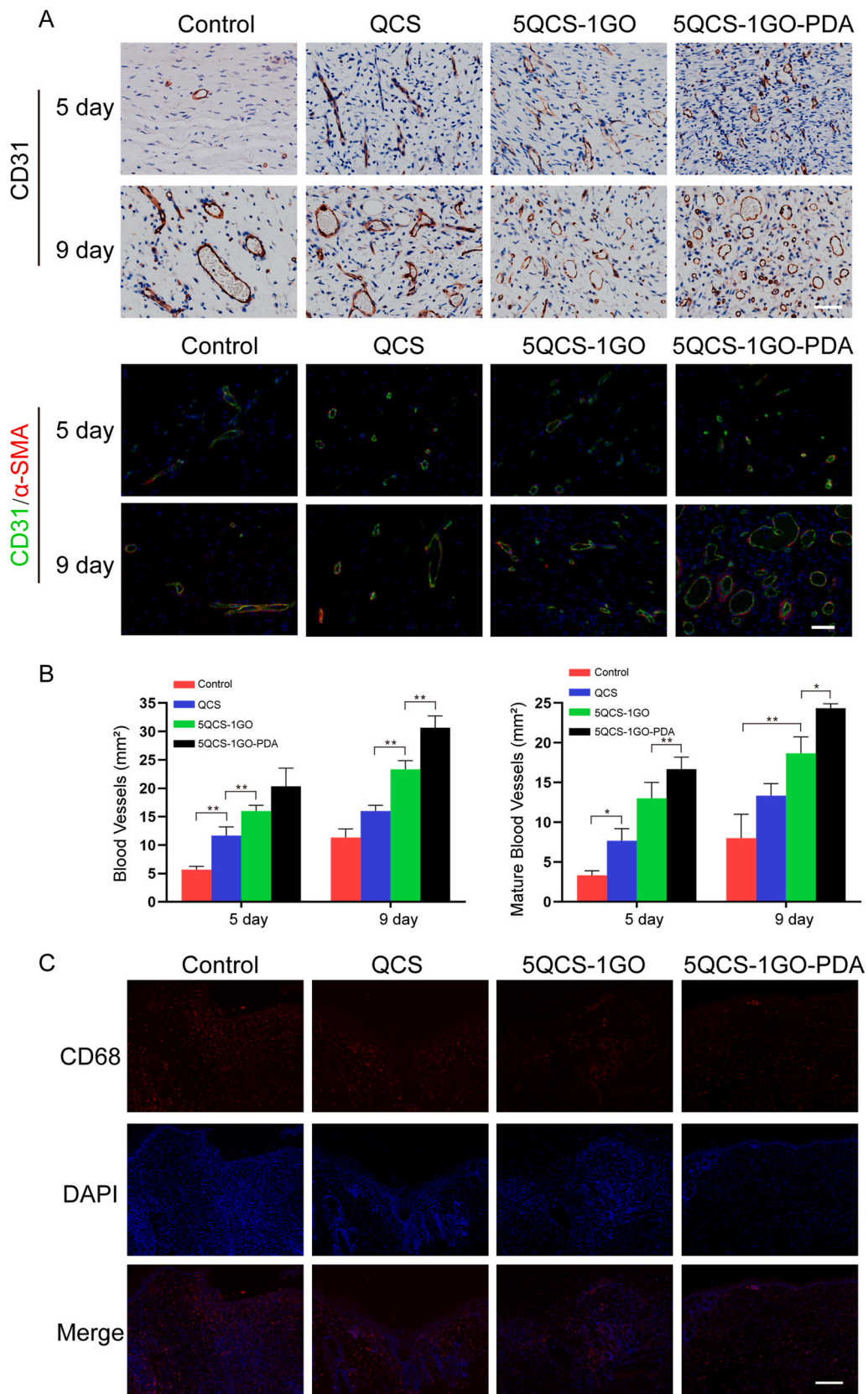
**Fig. 6.** Angiogenesis and inflammatory response at the wound site following treatment with nanohybrids at different time points. (A) Immunohistochemical staining of CD31 and co-location of CD31 and α-SMA immunofluorescence staining in the skin defect area at 5 and 9 days postoperatively. Scale bar: 50 μm. (B) Quantitative analysis of the number of newly-formed blood vessels and mature blood vessels in the control group and QCS/5QCS-1GO/5QCS-1GO-PDA at 5 and 9 days after operation. (C) CD68 immunofluorescence staining of the wound site in different treatment groups 5 days after surgery. Scale bar: 200 μm. Data are represented as mean ± SD ($n = 3$, $*p < 0.05$, $**p < 0.01$).
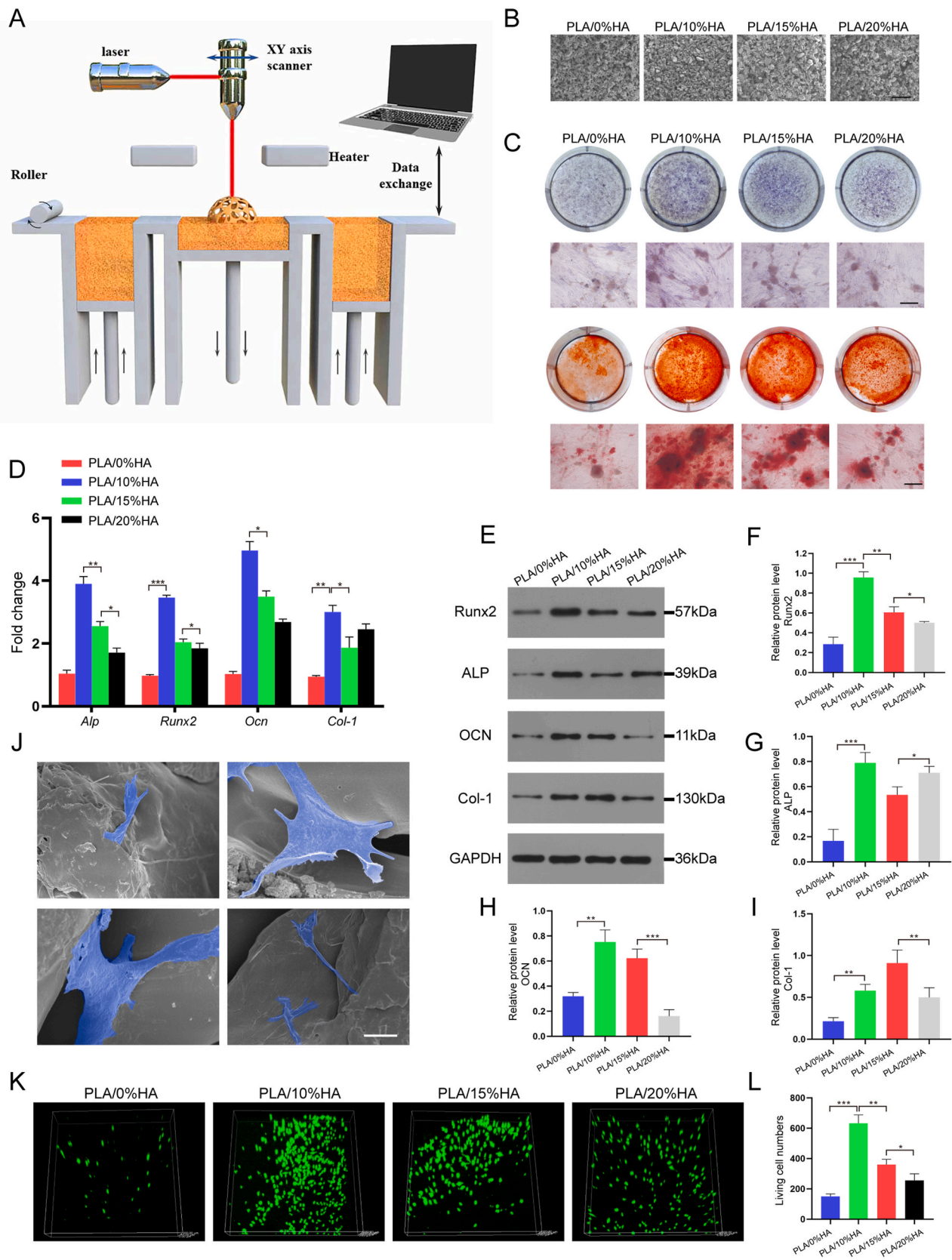
**Fig. 7.** Surface morphology, cell adhesion and osteogenic ability of the PLA/HA scaffolded by SLS. (A) Schematic diagram of PLA/HA scaffolds printed by SLS. (B) SEM images of the PLA/HA printed with different proportions with SLS. Scale bar: 500 μm. (C) Alkaline phosphatase and alizarin red staining of different proportions of the PLA/HA scaffolds. Scale bar: 100 μm. (D) qRT-PCR was used to detect the expression of osteogenic genes in MC3T3-E1 cells co-cultured with different proportions of PLA/HA scaffolds. (E–I) Western blotting of MC3T3-E1-associated osteogenic protein expression on PLA/HA scaffolds at different proportions. (J) MC3T3-E1 cells adhesion on the PLA/10%HA scaffold. Scale bar: 5 μm. (K–L) Confocal laser microscopic imaging of MC3T3-E1 cells cultured on the PLA/HA scaffolds staining at day 3 (green: live cells). Data are represented as mean ± SD ($n = 3$, $*p < 0.05$, $**p < 0.01$, $***p < 0.001$).
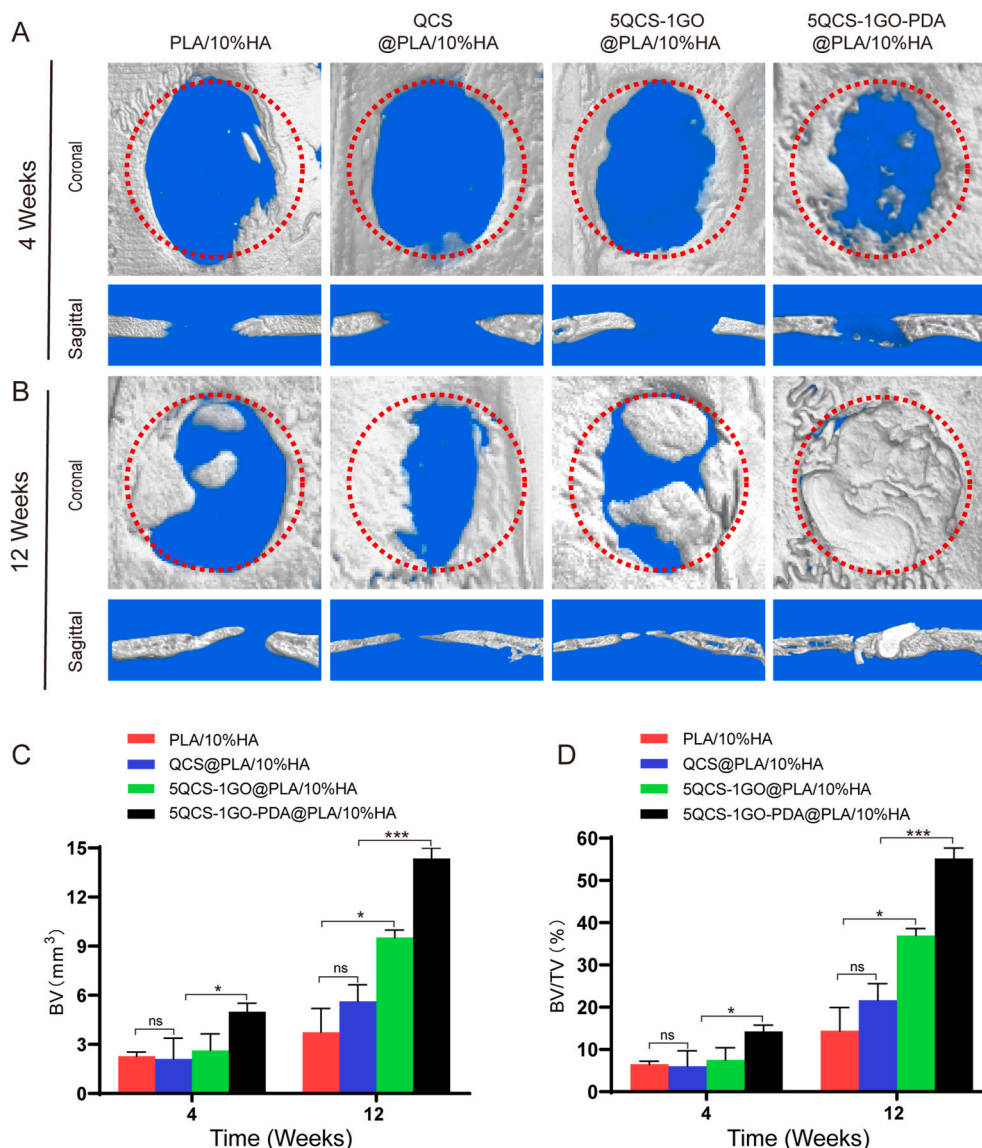
**Fig. 8.** Micro–CT imaging analysis of the critical size bone defect and repair in rats. (A–B) 3D reconstruction and coronal analysis of the defect area at 4 and 12 weeks. (C–D) Quantitative analysis of bone volume (BV) and bone volume/total volume (BV/TV) at 4 and 12 weeks in the different groups treated with composite scaffolds. Data are represented as mean ± SD ($n = 6$, $*p < 0.05$, $***p < 0.001$).

PDA@PLA/10%HA was 14 times and 30 times higher than that in control group at 4 and 12 weeks after surgery, respectively, suggesting that 5QCS-1GO-PDA@PLA/10%HA could significantly promote M2-type polarization of macrophages (Fig. S9B-C).

To further evaluate the osteogenic potential of the composite scaffolds, OCN expression was immunohistochemically assessed at 4 and 12 weeks after implantation (Fig. 10A) with brown areas indicating positive OCN expression. After 4 weeks of implantation, the positive area of QCS@PLA/10%HA group was lower than that of 5QCS-1GO@PLA/10% HA and 5QCS-1GO-PDA@PLA/10%HA group. At 12 weeks after scaffold implantation, new bone tissue appeared in the 5QCS-1GO@PLA/HA and 5QCS-1GO-PDA@PLA/HA groups, showing brown positive staining and distribution within the bone defect confirming that the novel bone tissue regenerated in the 5QCS-1GO@PLA/HA and 5QCS-1GO-PDA@PLA/HA groups.

### 2.7.1. *5QCS-1GO-PDA enhances osteogenic repair via the BMP2/BMPRs/Smads/Runx2 signaling pathway*

As shown in Fig. 10B-C, after treatment with 5QCS-1GO-PDA (0, 25, 50, 75 μg/mL) for 36 h, the expression of BMP2, BMPR1B, BMPR2, p-

Smad1/5/8, Smad1/5/8 and Runx2 proteins was detected by western blotting. The results showed that proteins in 5QCS-1GO-PDA stimulated cells were activated in a concentration-dependent manner at 36 h. This suggests that the BMP2/BMPRs/Smads/Runx2 signaling pathway is involved by 5QCS-1GO-PDA in the osteogenesis of MC3T3-E1 cells.

## 3. Discussion

Traumatic tissue damage is a common clinical encounter and access to multifunctional biomaterials that can concurrently repair skin and bone tissue damage has the potential to revolutionize medicine [22,23]. Creating a suitable microenvironment conducive to tissue repair at the initial stage of injury, which not only effectively prevents infection in the wound, but also helps initiate tissue repair and regeneration, is imperative. Although the effect of the three components, QCS, GO and PDA, when applied independently in the repair of skin injuries has been studied, there are few reports about investigating the combined effect of the components in bone defect repair [16,21]. In this study, we synthesized QCS-GO at different mass ratios by covalently grafting QCS and GO, and modified it with PDA to obtain QCS-GO-PDA. The results of our
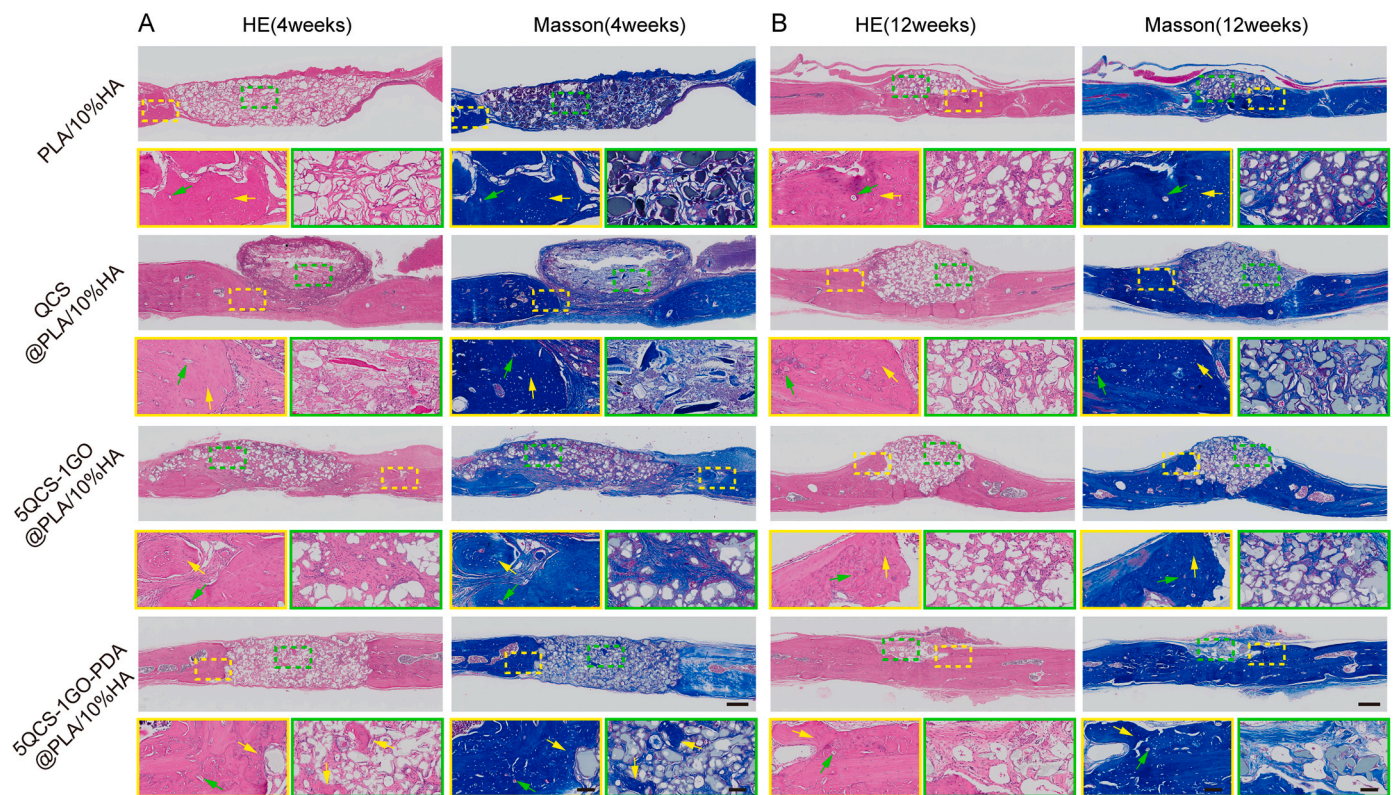
**Fig. 9.** H&E staining and Masson's trichrome staining at 4 and 12 weeks postoperatively to visualize *in vivo* repair of critical bone defects in the different groups treated with composite scaffolds. (A–B) The yellow box represents the edge of the defect area and the green box represents the center of the defect area (yellow arrow: new bone tissues; green arrow: blood vessels). Scale bar: 500 μm or 100 μm.

study showed that the nanohybrids with a mass ratio of 5:1 QCS to GO had both optimal biocompatibility and excellent antibacterial activity. The biological effects of the 5QCS-1GO-PDA were researched, including its antioxidation, osteogenic and vasogenic ability. In a full-thickness skin defect model in rats, 5QCS-1GO-PDA was able to promote wound closure and skin appendage regeneration. Subsequently, 5QCS-1GO-PDA was combined with a PLA/10%HA scaffold printed using SLS to treat a critical bone defect in rat skulls. The results showed that the 5QCS-1GO-PDA could accelerate bone regeneration via the BMP2/BMPRs/Smads/Runx2 signaling pathway.

Biomaterials for tissue repair should not only exert beneficial biological effects, but also have excellent antibacterial properties, so as to play a simultaneous role in anti-infection and promotion of tissue repair [24]. Angiogenesis is significant in tissue repair and regeneration, ensuring adequate perfusion and provision of oxygen and nutrients for the growth of structures in the defect tissue, as well as removal of metabolites that are not conducive to tissue growth [25]. It has been reported that GO can promote *in vitro* angiogenesis by activating phosphorylation, and the addition of PDA can reduce and modify GO, making it more appropriate for application in tissue engineering [21]. Previous studies have shown that GO alone has weak antibacterial abilities, while QCS, the most antibacterial derivative of chitosan, has strong antibacterial ability against both gram-positive and gram-negative bacteria [11,26]. In this study, the antibacterial results on the three types of bacteria showed that with an increase in the proportion of QCS, the antibacterial ability of QCS-GO-PDA nano-hybrid gradually increased, while the bactericidal rate tended to be stable for 5QCS-1GO-PDA. Our study also indicated that with the increasing proportion of QCS, QCS-GO-PDA nanohybrid showed higher biocompatibility. Addition of bioactive materials to GO through an amide bond can help reduce the cytotoxicity of GO, which surrounds the edges of GO in the compound, reducing the likelihood of physical damage to the cells

[26].

TGF-β/BMP2 is an important signaling pathway that promotes bone formation [27]. Furthermore, BMP2 binds to BMP2R in endothelial cells and promotes endothelial cell proliferation and angiogenesis through phosphorylation of Smad1/5/8 [28]. Immune regulation is a key characteristic that determines the ability of biomaterials to regulate the bone immune environment, which is in turn significant for tissue regeneration. Previous studies have shown that there is immune crosstalk between osteogenesis and angiogenesis [9,23]. Runx2, a common target of the TGF-β1/BMP2 signaling, is a key regulator of osteogenic differentiation and directly stimulates the transcriptional expression of osteogenic genes (ALP/Col-1/OCN) by binding to osteoblast-specific *cis*-acting element 2 (OSE2) [29]. VEGF is a powerful growth factor secreted by endothelial cells and stimulates blood vessel formation by binding to the corresponding receptor VEGFR [30]. Activation of VEGFR further stimulates downstream signaling pathways and promotes angiogenesis. VEGF can be upregulated in macrophages, and it synergistically promotes osteogenic differentiation with BMP2, thereby promoting osteogenesis through the BMP2 signaling pathway [31]. Previous studies have shown that BMP2 and TGF-β1 secreted by macrophages can bind to BMP2R and TGF-β1R in vascular endothelial cells, respectively, and phosphorylate Smad1/5/8 to promote endothelial cell proliferation and vascular formation [32]. The upregulation of PECAM and FGF can synergistically stimulate angiogenesis and maintain the normal physiological function of neovascularization [33]. In this study, we observed the synergistic effect between the immune microenvironment generated by macrophages activated by 5QCS-1GO-PDA, osteogenesis and angiogenesis, that is, TGF-β/BMP2, VEGF and other signaling pathways can be activated by establishing a good immune microenvironment to enhance osteogenesis and angiogenesis. Taken together, these findings suggest the importance of immunomodulatory biomaterials for the repair of damaged tissues.
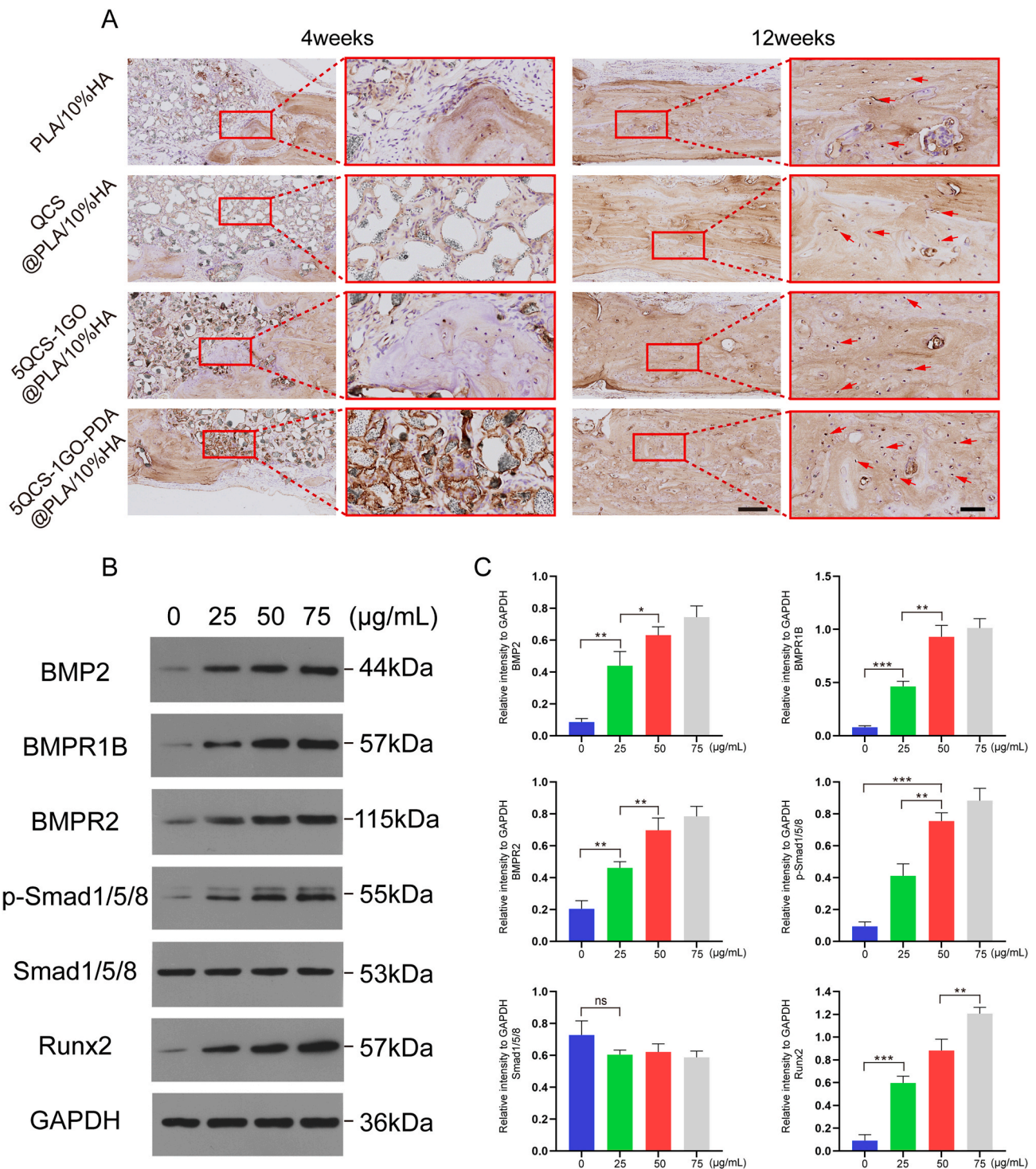
**Fig. 10.** Immunohistochemical staining of *in vivo* critical bone repair and validation of the signaling pathway of the osteogenic effect of nanohybrid 5QCS-1GO-PDA. (A) OCN-stained images were obtained at 4 weeks and 12 weeks after implantation, and brown positive staining (red arrows) was observed in bone lacunaes. (B–C) Western blotting was used to detect the expression of BMP2, BMPR1B, BMPR2, p-Smad1/5/8, Smad1/5/8 and Runx2 proteins in MC3T3-E1 cells treated with 5QCS-1GO-PDA (25, 50 and 75 μg/mL). All results were repeated three times. Scale bar: 250 μm or 50 μm. Data are represented as mean ± SD ($n = 3$, *$p < 0.05$, **$p < 0.01$, ***$p < 0.001$).

SLS is a significant technology in the field of 3D printing [34]. Compared with traditional processes, SLS allows personalized printing for different patients, and has broad application prospects in biological materials. Many studies have shown that SLS is a technology very suitable for the preparation of medical implants and tissue engineered scaffolds using biopolymer and its composite materials, which has numerous advantages, including custom structure design and great performance and biocompatibility of its products [35,36]. PLA is a biodegradable material, which can be 3D printed into tissue-engineered scaffolds. The composite of PLA with HA, the main component of bone matrix, can effectively improve the biological activity of scaffolds [37]. At present, there are relatively few studies investigating the use of SLS to form PLA composites, research on PLA/HA composites mainly revolves around injection molding or solution blending, and there are almost no

related studies on bone defects [38]. In this study, SLS technology was used to print PLA/HA composite scaffolds, and we found that PLA/HA composite scaffolds with HA mass fraction of 10% showed a higher number of living cells and enhanced osteogenic effect. In clinical practice, CT scan of patients' bone defects can be carried out first, and the data can be imported in DICOM format into automated modeling software. After the design results are evaluated and stabilized, the data can be exported in STL/AMF format, and the SLS technology can be used to print custom bone repair scaffolds that meet the needs of patients with different tissue defects. Benefiting from a variety of biological functions, 5QCS-1GO-PDA can be used as a coating material to increase the antibacterial, osteogenic and vasogenic abilities of PLA/10%HA, as well as free radical scavenging ability to promote the polarization of macrophages in a direction conducive to regeneration. Meanwhile, the alkaline environment of PDA allows neutralization of the acidic products produced during PLA degradation and reduces the inflammatory reaction to the implant.

The production of large amounts of free radicals impedes tissue repair through increased oxidative stress, DNA disruption caused by lipid peroxidation and enzyme inactivation [39]. PDA contains a large number of bioactive groups, including catecholamines, –OH and –NH$_2$, which contribute to apatite mineralization and cell attachment [21]. With PDA surface modification, the active ingredients can be fixed to the surface of bone scaffolds, so as to enable good cell affinity and osteogenic effects. PDA can effectively reduce inflammation and modulate the immune response to scaffolds [40]. These functions are reflected in immune regulation, which effectively inhibits inflammation, increases the number of new blood vessels, and decreases the ROS level in the defect tissue, helping to reduce inflammation and promote tissue regeneration [41]. In addition, PDA can improve the hydrophilicity of the material surface, thus significantly promoting cell adhesion and proliferation [42]. Some researchers have shown that PDA can form non-covalent and covalent bonds with almost all types of organic and inorganic materials through catechin functional groups at a weakly alkaline pH [43]. This is because a large number of active functional groups in PDA can interact with cell membrane cationic-π or π-π interaction to promote cell adhesion [16]. In our study, compared with the QCS and 5QCS-1GO, 5QCS-1GO-PDA showed stronger ROS scavenging ability, which could promote M2-type polarization of macrophages and cytokine secretion.

The surface of biological scaffolds is an important property to consider with regard to the interaction between biomaterials and cells [44,45]. As cell-biomaterial surface interactions can significantly affect cell behavior and function, biomimetic materials that mimic natural repair processes are of great interest [46]. In previous studies, multiple anabolic signaling pathways were identified to be involved in the regulation of bone formation, including the BMP2/Smads/Runx2 and Wnt/β-catenin pathways [47]. Multiple studies have identified the BMP2 signaling pathway as a clear and important positive regulatory pathway in bone homeostasis [28]. Previous studies have found that M2-type macrophages can participate in osteogenesis by releasing bone-inducing signals including BMP2 [32,48]. BMP receptors are known to activate the Smad1/5/8 signaling pathway, and phosphorylated Smad1/5/8 forms a complex with Smad4, which is transferred to the nucleus where it interacts with other transcription factors [47,49]. In this study, we found that 5QCS-1GO-PDA activated BMP2/Smads/-Runx2 signaling in a concentration-dependent manner, thereby promoting the expression of osteogenic genes, suggesting that 5QCS-1GO-PDA can serve as a surface modification coating for biological scaffolds to synergistically regulate osteogenic differentiation and promote osseointegration. However, there are several significant limitations to this study. Since the pathogenesis of infection is a complex process involving interactions between pathogens, hosts, and biomaterials, in our ongoing studies, tissue defect models with bacterial infection *in vivo* will be used to evaluate the effectiveness of nanohybrids and their modified composite scaffolds for tissue regeneration and

repair. In addition, it is also necessary to determine whether other immune cells are involved in the crosstalk effect of nanohybrids on osteogenesis and angiogenesis and the specific molecular mechanism.

## 4. Conclusion

In summary, we synthesized a nano-hybrid QCS-GO through covalent grafting of QCS and GO, and further modified it with PDA to obtain QCS-GO-PDA. The results indicated that 5QCS-1GO-PDA has a variety of functions including antibacterial, angiogenic and osteogenic abilities, and can induce M2-type macrophage polarization conducive to tissue regeneration and ROS elimination. Treatment of a full-layer defect model *in vivo* showed that 5QCS-1GO-PDA permits efficient wound healing and regeneration of skin appendages. 5QCS-1GO-PDA nanohybrid-modified PLA/10%HA played an important role in rapid bone regeneration of critical bone defects in rats through the BMP2/BMPRs/Smads/Runx2 signaling pathway. Overall, we found that 5QCS-1GO-PDA, a multifunctional nano-hybrid compound, can promote the repair of tissue defects by modulating the immune cross-talk between osteogenesis and angiogenesis, which provides a novel and promising feasible strategy for the clinical repair of tissue injuries.

## Declaration of competing interest

The authors declare no conflict of interest.

## CRediT authorship contribution statement

**Hang Xue:** Conceptualization, Data curation, Methodology, Writing – original draft. **Zhenhe Zhang:** Conceptualization, Data curation, Methodology, Writing – original draft. **Ze Lin:** Methodology, Formal analysis. **Jin Su:** Data curation. **Adriana C. Panayi:** Supervision, Writing – review & editing. **Yuan Xiong:** Visualization. **Liangcong Hu:** Investigation. **Yiqiang Hu:** Software, Visualization. **Lang Chen:** Methodology, Validation. **Chenchen Yan:** Validation, Data curation. **Xudong Xie:** Resources, Validation. **Yusheng Shi:** Supervision, Writing – review & editing. **Wu Zhou:** Supervision, Writing – review & editing. **Bobin Mi:** Writing – review & editing, Project administration. **Guohui Liu:** Writing – review & editing, Project administration.

## Appendix A. Supplementary data

Supplementary data related to this article can be found at https://doi.org/10.1016/j.bioactmat.2022.05.023.

## References

[1] T.A. Einhorn, L.C. Gerstenfeld, Fracture healing: mechanisms and interventions, Nat. Rev. Rheumatol. 11 (1) (2015) 45–54, https://doi.org/10.1038/nrrheum.2014.164.

[2] B. Kundu, R. Rajkhowa, S.C. Kundu, X. Wang, Silk fibroin biomaterials for tissue regenerations, Adv. Drug Deliv. Rev. 65 (4) (2013) 457–470, https://doi.org/10.1016/j.addr.2012.09.043.

[3] S.A. Eming, P. Martin, M. Tomic-Canic, Wound repair and regeneration: mechanisms, signaling, and translation, Sci. Transl. Med. 6 (265) (2014) 265sr6, https://doi.org/10.1126/scitranslmed.3009337.

[4] L. Bai, P. Chen, Y. Zhao, R. Hang, X. Yao, B. Tang, C. Liu, Y. Xiao, R. Hang, A micro/nano-biomimetic coating on titanium orchestrates osteo/angio-genesis and osteoimmunomodulation for advanced osseointegration, Biomaterials 278 (2021), 121162, https://doi.org/10.1016/j.biomaterials.2021.121162.

[5] B.N. Brown, B.D. Ratner, S.B. Goodman, S. Amar, S.F. Badylak, Macrophage polarization: an opportunity for improved outcomes in biomaterials and regenerative medicine, Biomaterials 33 (15) (2012) 3792–3802, https://doi.org/10.1016/j.biomaterials.2012.02.034.

[6] P. Qiu, M. Li, K. Chen, B. Fang, P. Chen, Z. Tang, X. Lin, S. Fan, Periosteal matrix-derived hydrogel promotes bone repair through an early immune regulation coupled with enhanced angio- and osteogenesis, Biomaterials 227 (2020), 119552, https://doi.org/10.1016/j.biomaterials.2019.119552.

[7] G.D. Marconi, F. Diomede, J. Pizzicannella, L. Fonticoli, I. Merciaro, S. D. Pierdomenico, E. Mazzon, A. Piattelli, O. Trubiani, Enhanced VEGF/VEGF-R and RUNX2 expression in human periodontal ligament stem cells cultured on sandblasted/etched titanium disk, Front. Cell Dev. Biol. 8 (2020) 315, https://doi.org/10.3389/fcell.2020.00315.

[8] W.H. Zuo, P. Zeng, X. Chen, Y.J. Lu, A. Li, J.B. Wu, Promotive effects of bone morphogenetic protein 2 on angiogenesis in hepatocarcinoma via multiple signal pathways, Sci. Rep. 6 (2016) 37499, https://doi.org/10.1038/srep37499.

[9] F. Diomede, G.D. Marconi, L. Fonticoli, J. Pizzicannella, I. Merciaro, P. Bramanti, E. Mazzon, O. Trubiani, Functional relationship between osteogenesis and angiogenesis in tissue regeneration, Int. J. Mol. Sci. 21 (9) (2020), https://doi.org/10.3390/ijms21093242.

[10] S.K. Ramasamy, A.P. Kusumbe, L. Wang, R.H. Adams, Endothelial Notch activity promotes angiogenesis and osteogenesis in bone, Nature 507 (7492) (2014) 376–380, https://doi.org/10.1038/nature13146.

[11] H. Xue, L. Hu, Y. Xiong, X. Zhu, C. Wei, F. Cao, W. Zhou, Y. Sun, Y. Endo, M. Liu, Y. Liu, J. Liu, A. Abududilibaier, L. Chen, Y. Can, B. Mi, G. Liu, Quaternized chitosan-Matrigel-polyacrylamide hydrogels as wound dressing for wound repair and regeneration, Carbohydr. Polym. 226 (2019), 115302, https://doi.org/10.1016/j.carbpol.2019.115302.

[12] R.C.H. Gresham, C.S. Bahney, J.K. Leach, Growth factor delivery using extracellular matrix-mimicking substrates for musculoskeletal tissue engineering and repair, Bioact. Mater. 6 (7) (2021) 1945–1956, https://doi.org/10.1016/j.bioactmat.2020.12.012.

[13] J.R. Xavier, T. Thakur, P. Desai, M.K. Jaiswal, N. Sears, E. Cosgriff-Hernandez, R. Kaunas, A.K. Gaharwar, Bioactive nanoengineered hydrogels for bone tissue engineering: a growth-factor-free approach, ACS Nano 9 (3) (2015) 3109–3118, https://doi.org/10.1021/nn507488s.

[14] K.S. Lee, J. Lee, H.K. Kim, S.H. Yeom, C.H. Woo, Y.J. Jung, Y.E. Yun, S.Y. Park, J. Han, E. Kim, J.H. Sul, J.M. Jung, J.H. Park, J.S. Choi, Y.W. Cho, D.G. Jo, Extracellular vesicles from adipose tissue-derived stem cells alleviate osteoporosis through osteoprotegerin and miR-21-5p, J. Extracell. Vesicles 10 (12) (2021), e12152, https://doi.org/10.1002/jev2.12152.

[15] Z.X. Peng, L. Wang, L. Du, S.R. Guo, X.Q. Wang, T.T. Tang, Adjustment of the antibacterial activity and biocompatibility of hydroxypropyltrimethyl ammonium chloride chitosan by varying the degree of substitution of quaternary ammonium, Carbohydr. Polym. 81 (2) (2010) 275–283, https://doi.org/10.1016/j.carbpol.2010.02.008.

[16] M. Li, Y.P. Liang, J.H. He, H.L. Zhang, B.L. Guo, Two-pronged strategy of biomechanically active and biochemically multifunctional hydrogel wound dressing to accelerate wound closure and wound healing, Chem. Mater. 32 (23) (2020) 9937–9953, https://doi.org/10.1021/acs.chemmater.0c02823.

[17] C. Zhou, S. Liu, J. Li, K. Guo, Q. Yuan, A. Zhong, J. Yang, J. Wang, J. Sun, Z. Wang, Collagen functionalized with graphene oxide enhanced biomimetic mineralization and in situ bone defect repair, ACS Appl. Mater. Interfaces 10 (50) (2018) 44080–44091, https://doi.org/10.1021/acsami.8b17636.

[18] W. Cheng, X. Zeng, H. Chen, Z. Li, W. Zeng, L. Mei, Y. Zhao, Versatile polydopamine platforms: synthesis and promising applications for surface modification and advanced nanomedicine, ACS Nano 13 (8) (2019) 8537–8565, https://doi.org/10.1021/acsnano.9b04436.

[19] A. Awad, F. Fina, A. Goyanes, S. Gaisford, A.W. Basit, Advances in powder bed fusion 3D printing in drug delivery and healthcare, Adv. Drug Deliv. Rev. 174 (2021) 406–424, https://doi.org/10.1016/j.addr.2021.04.025.

[20] D. da Silva, M. Kaduri, M. Poley, O. Adir, N. Krinsky, J. Shainsky-Roitman, A. Schroeder, Biocompatibility, biodegradation and excretion of polylactic acid (PLA) in medical implants and theranostic systems, Chem. Eng. J. 340 (2018) 9–14, https://doi.org/10.1016/j.cej.2018.01.010.

[21] P. Tang, L. Han, P. Li, Z. Jia, K. Wang, H. Zhang, H. Tan, T. Guo, X. Lu, Mussel-Inspired electroactive and antioxidative scaffolds with incorporation of polydopamine-reduced graphene oxide for enhancing skin wound healing, ACS Appl. Mater. Interfaces 11 (8) (2019) 7703–7714, https://doi.org/10.1021/acsami.8b18931.

[22] B. Ferrigno, R. Bordett, N. Duraisamy, J. Moskow, M.R. Arul, S. Rudraiah, S. P. Nukavarapu, A.T. Vella, S.G. Kumbar, Bioactive polymeric materials and electrical stimulation strategies for musculoskeletal tissue repair and regeneration, Bioact. Mater. 5 (3) (2020) 468–485, https://doi.org/10.1016/j.bioactmat.2020.03.010.

[23] D. Jiao, A. Zheng, Y. Liu, X. Zhang, X. Wang, J. Wu, W. She, K. Lv, L. Cao, X. Jiang, Bidirectional differentiation of BMSCs induced by a biomimetic procallus based on a gelatin-reduced graphene oxide reinforced hydrogel for rapid bone regeneration, Bioact. Mater. 6 (7) (2021) 2011–2028, https://doi.org/10.1016/j.bioactmat.2020.12.003.

[24] R. Yang, G. Li, C. Zhuang, P. Yu, T. Ye, Y. Zhang, P. Shang, J. Huang, M. Cai, L. Wang, W. Cui, L. Deng, Gradient bimetallic ion-based hydrogels for tissue microstructure reconstruction of tendon-to-bone insertion, Sci. Adv. 7 (26) (2021), https://doi.org/10.1126/sciadv.abg3816.

[25] Y. Aghazadeh, S.T. Khan, B. Nkennor, S.S. Nunes, Cell-based therapies for vascular regeneration: past, present and future, Pharmacol. Ther. 231 (2022), 107976, https://doi.org/10.1016/j.pharmthera.2021.107976.

[26] Y. Wang, A.G. El-Deen, P. Li, B.H. Oh, Z. Guo, M.M. Khin, Y.S. Vikhe, J. Wang, R. G. Hu, R.M. Boom, K.A. Kline, D.L. Becker, H. Duan, M.B. Chan-Park, High-performance capacitive deionization disinfection of water with graphene oxide-graft-quaternized chitosan nanohybrid electrode coating, ACS Nano 9 (10) (2015) 10142–10157, https://doi.org/10.1021/acsnano.5b03763.

[27] U. Ripamonti, R. Duarte, C. Ferretti, Re-evaluating the induction of bone formation in primates, Biomaterials 35 (35) (2014) 9407–9422, https://doi.org/10.1016/j.biomaterials.2014.07.053.

[28] P. Wang, L. Zhang, J. Yao, Y. Shi, P. Li, K. Ding, An arabinogalactan from flowers of Panax notoginseng inhibits angiogenesis by BMP2/Smad/Id1 signaling, Carbohydr. Polym. 121 (2015) 328–335, https://doi.org/10.1016/j.carbpol.2014.11.073.

[29] K. Nakashima, X. Zhou, G. Kunkel, Z. Zhang, J.M. Deng, R.R. Behringer, B. de Crombrugghe, The novel zinc finger-containing transcription factor osterix is required for osteoblast differentiation and bone formation, Cell 108 (1) (2002) 17–29, https://doi.org/10.1016/s0092-8674(01)00622-5.

[30] P. Carmeliet, Angiogenesis in life, disease and medicine, Nature 438 (7070) (2005) 932–936, https://doi.org/10.1038/nature04478.

[31] A. Gangopahyay, M. Oran, E.M. Bauer, J.W. Wertz, S.A. Comhair, S.C. Erzurum, P. M. Bauer, Bone morphogenetic protein receptor II is a novel mediator of endothelial nitric-oxide synthase activation, J. Biol. Chem. 286 (38) (2011) 33134–33140, https://doi.org/10.1074/jbc.M111.274100.

[32] X. Wang, S. Abraham, J.A.G. McKenzie, N. Jeffs, M. Swire, V.B. Tripathi, U.F. O. Luhmann, C.A.K. Lange, Z. Zhai, H.M. Arthur, J. Bainbridge, S.E. Moss, J. Greenwood, LRG1 promotes angiogenesis by modulating endothelial TGF-β signalling, Nature 499 (7458) (2013) 306–311, https://doi.org/10.1038/nature12345.

[33] M. Joner, G. Nakazawa, A.V. Finn, S.C. Quee, L. Coleman, E. Acampado, P. S. Wilson, K. Skorija, Q. Cheng, X. Xu, H.K. Gold, F.D. Kolodgie, R. Virmani, Endothelial cell recovery between comparator polymer-based drug-eluting stents, J. Am. Coll. Cardiol. 52 (5) (2008) 333–342, https://doi.org/10.1016/j.jacc.2008.04.030.

[34] A. Kafle, E. Luis, R. Silwal, H.M. Pan, P.L. Shrestha, A.K. Bastola, 3D/4D printing of polymers: fused deposition modelling (FDM), selective laser sintering (SLS), and stereolithography (SLA), Polymers 13 (18) (2021), https://doi.org/10.3390/polym13183101.

[35] F. Fina, A. Goyanes, S. Gaisford, A.W. Basit, Selective laser sintering (SLS) 3D printing of medicines, Int. J. Pharm. 529 (1–2) (2017) 285–293, https://doi.org/10.1016/j.ijpharm.2017.06.082.

[36] Y.A. Gueche, N.M. Sanchez-Ballester, S. Cailleaux, B. Bataille, I. Soulairol, Selective laser sintering (SLS), a new chapter in the production of solid oral forms (SOFs) by 3D printing, Pharmaceutics 13 (8) (2021), https://doi.org/10.3390/pharmaceutics13081212.

[37] W. Chen, L. Nichols, F. Brinkley, K. Bohna, W. Tian, M.W. Priddy, L.B. Priddy, Alkali treatment facilitates functional nano-hydroxyapatite coating of 3D printed polylactic acid scaffolds, Mater Sci Eng C Mater Biol Appl 120 (2021), 111686, https://doi.org/10.1016/j.msec.2020.111686.

[38] X. Zhao, Y. Han, J. Li, B. Cai, H. Gao, W. Feng, S. Li, J. Liu, D. Li, BMP-2 immobilized PLGA/hydroxyapatite fibrous scaffold via polydopamine stimulates osteoblast growth, Mater Sci Eng C Mater Biol Appl 78 (2017) 658–666, https://doi.org/10.1016/j.msec.2017.03.186.

[39] Y.Q. Hu, B. Wu, Y. Xiong, R.Y. Tao, A.C. Panayi, L. Chen, W.Q. Tian, H. Xue, L. Shi, X.L. Zhang, L.M. Xiong, B.B. Mi, G.H. Liu, Cryogenic 3D printed hydrogel scaffolds loading exosomes accelerate diabetic wound healing, Chem. Eng. J. 426 (2021) 17, https://doi.org/10.1016/j.cej.2021.130634.

[40] M. Mittal, M.R. Siddiqui, K. Tran, S.P. Reddy, A.B. Malik, Reactive oxygen species in inflammation and tissue injury, Antioxidants Redox Signal. 20 (7) (2014) 1126–1167, https://doi.org/10.1089/ars.2012.5149.

[41] T. Li, H. Ma, H. Ma, Z. Ma, L. Qiang, Z. Yang, X. Yang, X. Zhou, K. Dai, J. Wang, Mussel-Inspired nanostructures potentiate the immunomodulatory properties and angiogenesis of mesenchymal stem cells, ACS Appl. Mater. Interfaces 11 (19) (2019) 17134–17146, https://doi.org/10.1021/acsami.8b22017.

[42] K.Y. Lu, P.Y. Lin, E.Y. Chuang, C.M. Shih, T.M. Cheng, T.Y. Lin, H.W. Sung, F.L. Mi, H(2)O(2)-Depleting and O(2)-generating selenium nanoparticles for fluorescence imaging and photodynamic treatment of proinflammatory-activated macrophages, ACS Appl. Mater. Interfaces 9 (6) (2017) 5158–5172, https://doi.org/10.1021/acsami.6b15515.

[43] P. Feng, S. Peng, C. Shuai, C. Gao, W. Yang, S. Bin, A. Min, In situ generation of hydroxyapatite on biopolymer particles for fabrication of bone scaffolds owning bioactivity, ACS Appl. Mater. Interfaces 12 (41) (2020) 46743–46755, https://doi.org/10.1021/acsami.0c13768.

[44] H. Lee, S.M. Dellatore, W.M. Miller, P.B. Messersmith, Mussel-inspired surface chemistry for multifunctional coatings, Science (New York, N.Y.) 318 (5849) (2007) 426–430, https://doi.org/10.1126/science.1147241.

[45] R.J. Miron, D.D. Bosshardt, OsteoMacs: key players around bone biomaterials, Biomaterials 82 (2016) 1–19, https://doi.org/10.1016/j.biomaterials.2015.12.017.

[46] Y. Li, Y. Xiao, C. Liu, The horizon of materiobiology: a perspective on material-guided cell behaviors and tissue engineering, Chem. Rev. 117 (5) (2017) 4376–4421, https://doi.org/10.1021/acs.chemrev.6b00654.

[47] M. Majidinia, A. Sadeghpour, B. Yousefi, The roles of signaling pathways in bone repair and regeneration, J. Cell. Physiol. 233 (4) (2018) 2937–2948, https://doi.org/10.1002/jcp.26042.

[48] L. Bai, Z. Du, J. Du, W. Yao, J. Zhang, Z. Weng, S. Liu, Y. Zhao, Y. Liu, X. Zhang, X. Huang, X. Yao, R. Crawford, R. Hang, D. Huang, B. Tang, Y. Xiao, A multifaceted coating on titanium dictates osteoimmunomodulation and osteo/angio-genesis

towards ameliorative osseointegration, Biomaterials 162 (2018) 154–169, https://doi.org/10.1016/j.biomaterials.2018.02.010.

[49] S. Ruiz, H. Zhao, P. Chandakkar, J. Papoin, H. Choi, A. Nomura-Kitabayashi, R. Patel, M. Gillen, L. Diao, P.K. Chatterjee, M. He, Y. Al-Abed, P. Wang, C.N. Metz, S.P. Oh, L. Blanc, F. Campagne, P. Marambaud, Correcting Smad1/5/8, mTOR, and VEGFR2 treats pathology in hereditary hemorrhagic telangiectasia models, J. Clin. Invest. 130 (2) (2020) 942–957, https://doi.org/10.1172/jci127425.